UCRL-11513

UNIVERSITY OF CALIFORNIA

Lawrence Radiation Laboratory
Berkeley, California

AEC Contract No. W-7405-eng-48

LIQUID-SOLID TRANSFORMATION KINETICS IN ALUMINUM OXIDE

Amio R. Das
(Ph. D. Thesis)

July 15, 1964

Printed in USA. Price [redacted]. Available from the
Office of Technical Services
U. S. Department of Commerce
Washington 25, D.C.

DISCLAIMER

LIQUID-SOLID TRANSFORMATION KINETICS IN ALUMINUM OXIDE

Contents

LIQUID-SOLID TRANSFORMATION KINETICS IN ALUMINUM OXIDE

Amio R. Das

Inorganic Materials Research Division, Lawrence Radiation Laboratory, and Department of Nuclear Engineering, College of Engineering, University of California, Berkeley, California

July 15, 1964

ABSTRACT

A direct-current-arc plasma torch was used to subject sized particles of synthetic sapphire in the range of 9 to 124 microns to rapid melting and resolidification. The spherical particles resulting from the solidification of completely molten droplets were separated from the partially melted particles in order to study the formation of metastable crystalline phases of alumina from the liquid droplets subjected to rapid cooling. A fraction of these spheroidized particles showed various degrees of bubble formation.

The size and apparent density of the spheroidized particles and the ambient temperature conditions experienced by the liquid droplets during cooling were used as parameters in determining quenching rates. A hypothesis based on the kinetics of nucleation of the crystalline solid phases from the supercooled liquid droplets is proposed to explain the ratio of metastable phases to the stable α phase. Experimental data relating this ratio with quench rates of the liquid droplets show reasonable agreement with the proposed hypothesis.

I. INTRODUCTION

In many fundamental studies of ceramic systems, uniformly sized single-crystal particles have been used. In analyzing the results of such studies, the geometric shape of the particles presents problems that are not always resolved by assuming these random-shaped particles to be spheres. Thus, the need for spherical particles has always been felt. In recent years spherical particles have been produced by various means. Mechanical devices such as grinding have yielded single-crystal spheres in the millimeter range but are not capable of producing spheres in the micron range. These techniques are unsuitable for the production of comparatively larger quantities of spheres for experimental purposes. Flame melting techniques using both oxygen-hydrogen torches[1] and in recent years the direct-current-arc plasma jets[2] have been used to produce spheroidized particles of a large number of high-melting-temperature metals, metal oxides, metal carbides, etc. But the problem of producing single-crystal spheres in the range of 1 to 100 microns has remained unsolved.

A crystalline sphere can be made by allowing a liquid droplet of the material to solidify. However, to achieve a single crystal the nucleation and grain growth characteristics must be such that when one nucleus is formed, it immediately grows to convert the whole sphere volume to a solid. High grain-growth rates of crystalline phases require the fluidity of the liquid to be high. Metal droplets have been converted to single crystals in this manner.[3] The fluidity of molten aluminum oxide, an important ceramic, is comparatively high.[4] Therefore, an attempt was made to produce single-crystal aluminum oxide spheres in the range of 10 to 100 μ by the use of a direct-current plasma jet as the heat source.

Aluminum oxide has been spheroidized in both oxygen-hydrogen torches[1] and in direct-current-arc plasma jets.[2] Flame spraying of alumina coatings on both a commercial and laboratory scale has also used these two devices.[2,5] During these processes both stable α alumina and metastable phases of alumina have been observed in the melted and resolidified material.

Alumina has one stable phase, α, between room temperature and its melting point.[6] X-ray diffraction studies up to 2000°C have not shown the existence of a high-temperature modification.[7] Various metastable phases of near anhydrous or anhydrous alumina (γ, δ, θ, κ, χ, and η) have been identified.[6, 8, 9] Most of these phases are formed by the decomposition of various alumina salts such as hydrates, sulfates, nitrates, etc. In the absence of stabilizing impurities, the metastable phases are all converted to α-Al_2O_3 at approximately 1200°C. When α-Al_2O_3 is heated above 2000°C, it has been reported that a highly defective structure is formed.[10] This has been interpreted to be the result of structural breakdown near the melting point, as has been observed in a number of crystalline solids,[11a] and not as the formation of a new phase.

Plummer[1] in spheroidization studies using an oxygen-hydrogen flame hypothesized that metastable solid phases would be formed from the liquid because of the greater mobility of aluminum ions relative to the oxygen ions in the crystal and the possible decreased coordination number of aluminum ions in the liquid.

The liquid can be thought to contain most aluminum ions in tetrahedral coordination with the oxygen ions, while a small fraction are also in octahedral coordination, the latter being in the lower free-energy state. During cooling, these tetrahedral and octahedral groups of oxygen ions could first pack into a double layer of close-packed ions. With slow cooling, the aluminum ions in such a layer, due to their greater mobility, could move to the lower energy octahedral positions. The third and subsequent layers of close-packed oxygen ions could then be added so that the aluminum ions continued to move into octahedral positions, resulting finally in a corundum structure of the α phase. In case of rapid cooling, however, no time for the rearrangement of the aluminum ions would be available, and tetrahedral groups of oxygen ions would be quenched in from the liquid to result in approximately cubic close-packed structures, characteristic of the metastable phases of alumina.

In this investigation the kinetics of nucleation and growth of metastable and stable α alumina phases, resulting from the

thermodynamic driving forces, is suggested as being the controlling factor in determining the crystalline phase present after solidification of a liquid droplet. It is also observed that a suitably controlled, slow rate of cooling of the liquid droplets results in formation of single-crystal spheres of the α phase.

II. THEORY

A. Steady-State Nucleation

The free-energy relationships between a liquid and two crystalline solid phases are diagrammatically illustrated in Fig. 1. The lowest free energy determines the stable phase at any equilibrium temperature, T. If one solid phase, A, has its free energy related to that of the liquid as shown, then the other solid phase, B, may appear as a stable phase at high temperatures or be at all times unstable relative to A. These two conditions are represented by the two dashed curves. When B is stable at high temperatures, the transformation (A → B) occurs and B is known as the high-temperature phase. The intersection of the B curve with the free energy curve for the liquid is the equilibrium melting temperature of the solid, $T_{m_{B1}}$. When B is unstable relative to A, a pseudo melting temperature of B, $T_{m_{B2}}$, is evident as shown, and T_{m_A} is the equilibrium melting temperature of the crystalline solid.

For alumina, where the alpha phase is reported stable up to the melting point, each of the metastable phases of interest in this study (θ, δ, and γ) has a pseudo melting temperature lower than that of the alpha phase. The free-energy relationship of each of these metastable phases behaves as shown by the upper dashed curve of Fig. 1.

Classical theory of homogeneous nucleation as developed by Volmer, Becker, and Doring[12] and applied to the liquid-solid transition gives the steady-state nucleation rate as

$$I = n\, n_s^* \frac{kT}{h} \exp\left[\frac{-16\,\pi\,\sigma^3\,T_m^2}{3\,kT\,(T_m - T)^2\,\Delta H_f^2} - \frac{E_n}{kT}\right]. \qquad (1)$$

Here I is the number of nuclei appearing per cm^3-sec, n is the number of molecules per cm^3 of liquid, n_s^* is the number of molecules on the surface of a stable nucleus, σ is the solid-liquid interface energy in $ergs/cm^2$, ΔH_f is the volumetric heat of fusion in $ergs/cm^3$, k is Boltzmann's constant, h is Planck's constant, T_m is the equilibrium melting temperature in °K, T is the actual liquid temperature in °K where nucleation is occurring, E_n is the activation energy for diffusion

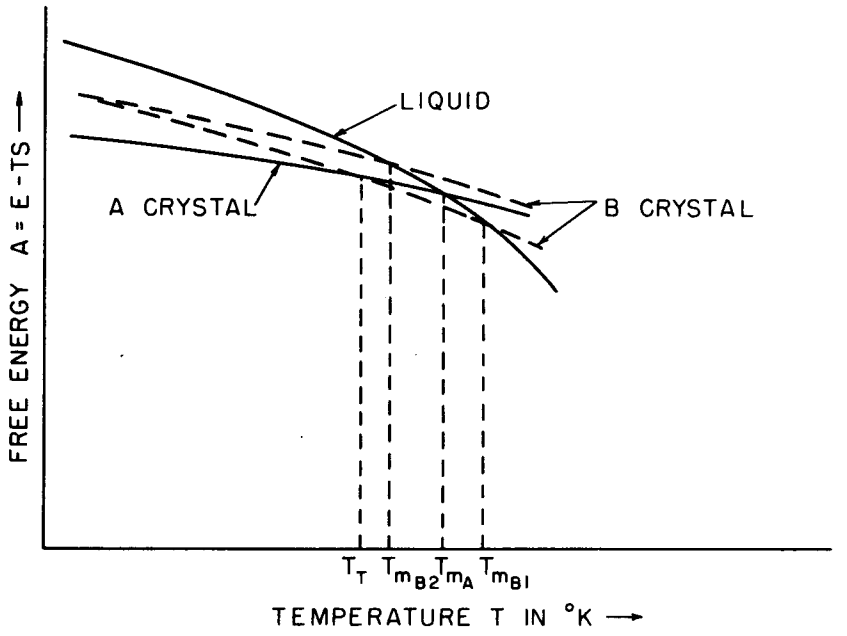

Fig. 1. Plot of free energy vs temperature for the liquid and two solid crystalline phases, A and B, of a substance.

in the liquid, which for convenience may be taken as the activation energy for viscosity in liquid alumina,[4] and $(T_m - T)$ is the degree of supercooling.

If there exists the possibility of nucleation of two different solid crystalline phases (a, the stable species, and m, a metastable species) which have different constants σ, T_m, and ΔH_f in Eq. (1), then the relationship of the nucleation rate vs temperature between these two phases may be as shown in Fig. 2a. The metastable phase may have a nucleation rate as shown by I'_m, which is always lower than I_a unless I_m crosses I_a as shown. For the latter case, at temperatures above T_c the nucleation of a is favored, and below T_c the nucleation of m is favored. In the case of several metastable species, several curves corresponding to different species may be drawn as in Fig. 2b. Under equilibrium conditions, the relative values of I at any temperature T determines the nucleation probabilities of the species m_1, m_2, m_3, etc. Appendix I.A gives a calculation based on known and assumed values of the constants in Eq. (1) and lends reasonable credibility to the above assumptions for the nucleation of crystals in liquid aluminum oxide.

B. Non-Steady-State Nucleation

When used to melt and spheroidize a crystalline feed, the dc plasma jet imposes dynamic conditions such that the exact time-temperature history is impossible to determine. Furthermore, Eq. (1) is the "steady-state" solution of the more general time-dependent equation describing nucleation of a solid crystalline phase from a liquid.[11b] However, Hillig[13] and Kantrowitz[14] showed that, in the more general time-dependent solution, the fluidity of the liquid determines the time for the higher transients to subside and for the "steady-state" condition to be attained. Similar calculations made in Appendix I.B indicate that the "steady-state" nucleation rate should be attained in less than 1 μsec. On the other hand, estimates based on photographic measurement of the velocity of the particles emerging from the plasma jet indicate that particles are subjected to a heating and cooling cycle of approximately 1 msec, the cooling period making the major contribution.

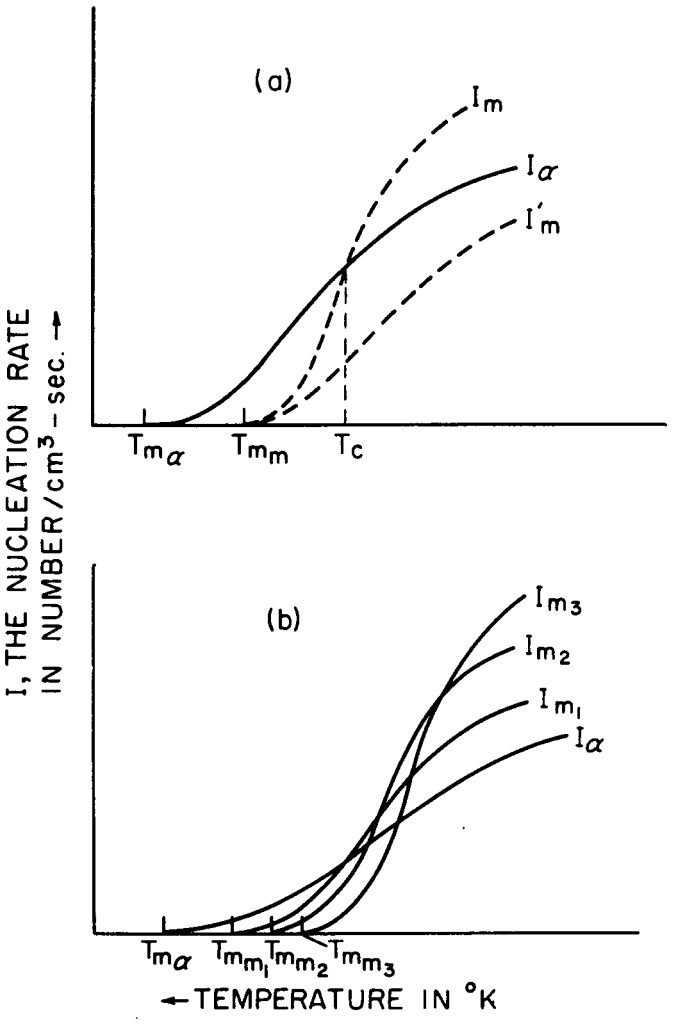

Fig. 2. Plot of nucleation rate vs temperature for (a) two solidifying phases, α and m, and (b) several solidifying phases, m_i and α.

Therefore, Eq. (1) may be used to explain the existence of metastable phases provided the temperature, T, be replaced by an estimated function of time T(t). This estimation can be based on the calculated heat-transfer characteristics of a liquid droplet.

Consider a drop of liquid of volume v, cooling down from a temperature above its melting point in such a manner that as soon as n nuclei of a crystalline solid phase appear, they grow at a rate, G_v, sufficient so that the drop is totally converted to the solid before further nucleation occurs. Then n, the number of crystals in the solid, is given by

$$n = \frac{v}{G_v \bar{\tau}} \geq 1, \tag{3}$$

where v is the volume of the liquid drop in cm^3, G_v is the volumetric growth rate per nucleus in cm^3/sec, and $\bar{\tau}$ is a small but finite time interval during which the solidification process is completed. Therefore, $v/n = G_v \bar{\tau}$ is the average grain size in cm^3 in the solidified droplet.

If (a) the growth rate, G_v, of a particular crystalline phase after nucleation has begun, is constant over the temperature range through which the droplets begin and complete the solidification process; and (b) the average time, $\bar{\tau}$, required for the liquid to be converted to a particular phase, is also constant, then $G_v \bar{\tau} = v/n$ can be assumed to be constant. For liquids of low viscosity, assumption (a) is reasonable, and calculations (Appendix II.A) show that $\bar{\tau}$ is not likely to vary much with particle size in the range of interest.

Let N be the number of cooling liquid droplets at a time, t, after all droplets are at a reference temperature, for example T_m. Then we define a function of time, F(t), such that

$$N = N_0 F(t), \tag{4}$$

where N_0 is the number of liquid droplets at $t = 0$, $F(t) = 1$ at $t = 0$, and $F(t) = 0$ at $t = \infty$.

Since the rate of solidification of the liquid drops equals their rate of disappearance from the liquid state, then in a small interval dt

about t, the volume of liquid drops disappearing by solidification equals the rate of solidification multiplied by the time interval, dt; or

$$-dN = I(t)\, N(t)\, \frac{v}{n}\, dt. \tag{5}$$

Here I(t) is the number of nuclei appearing per cm^3-sec, N(t) is the number of liquid droplets of equal size, v is the volume of a liquid droplet in cm^3, n is the number of nuclei required to convert the droplet to a solid, and

$$-\frac{dN}{dt} = IN\, \frac{v}{n}. \tag{6}$$

Differentiating Eq. (4) and equating it to (6), with the sign changed, we get

$$N_0\, \frac{d}{dt}\, F(t) = -IN\, \frac{v}{n}. \tag{7}$$

From (4) and (7) we get

$$N_0\, \frac{d}{dt}\, F(t) = -IN_0\, \frac{v}{n}\, F(t). \tag{8}$$

Integrating and applying initial conditions we get

$$F = \exp\left[-\frac{v}{n} \int_0^t I(z)dz\right]. \tag{9}$$

If both a stable species α and a metastable species m can nucleate from the liquid, then the total nucleation rate I(t) is given by the sum of the respective nucleation rates

$$I(t) = I_\alpha(t) + I_m(t). \tag{10}$$

Also the function F(t) is of the form

$$F(t) = F_\alpha(t)\, F_m(t) \tag{11}$$

so that

$$N = N_0\, F(t) = N_0\, F_\alpha(t)\, F_m(t). \tag{12}$$

Let us define N_α and N_m as number of solid droplets of phases α and m, respectively, and assume that one liquid droplet solidifies into one particular phase, since the estimated growth rates (Appendix II.A) are very rapid.

Then the number of drops of α phase formed is given by

$$dN_\alpha = I_\alpha N \frac{v}{n_\alpha} dt, \tag{13a}$$

where N is the total number of liquid droplets, v is the volume of each droplet, n_α is the number of nuclei of α phase appearing before the whole drop is converted to α phase, and

$$dN_m = I_m N \frac{v}{n_m} dt. \tag{13b}$$

From Eq. (9) we write

$$F = \exp\left[-\frac{v}{\bar{n}} \int_0^t I(z)dz\right], \tag{14}$$

where $\bar{n}$ is an average number such that

$$I \frac{v}{\bar{n}} = I_\alpha \frac{v}{n_\alpha} + I_m \frac{v}{n_m}. \tag{15}$$

Then from (14) and (15) we have

$$F = \exp\left[-\frac{v}{n_\alpha} \int_0^t I_\alpha(z)dz\right] \exp\left[-\frac{v}{n_m} \int_0^t I_m(z)dz\right]$$

$$= F_\alpha F_m,$$

as defined in Eq. (11). Therefore, from (13a) and (13b) we can write

$$\frac{dN_\alpha}{dt} = I_\alpha \frac{v}{n_\alpha} N_0 F(t) = N_0 \frac{v}{n_\alpha} I_\alpha F_\alpha F_m$$

$$= N_0 \frac{v}{n_\alpha} I_\alpha \exp\left[-v \int_0^t \left(\frac{I_\alpha(z)}{n_\alpha} + \frac{I_m(z)}{n_m}\right)dz\right]. \tag{16}$$

Integrating Eq. (16) and taking limits from $t = 0$ to $t = \infty$, we have

$$\frac{N_\alpha}{N_0}\Bigg|_0^\infty = \int_0^\infty \frac{v}{n_\alpha} I_\alpha(t) \exp\left[-v \int_0^t \left(\frac{I_\alpha(z)}{n_\alpha} + \frac{I_m(z)}{n_m}\right)dz\right] dt, \tag{17a}$$

and similarly

$$\frac{N_m}{N_0}\Bigg|_0^\infty = \int_0^\infty \frac{v}{n_m} I_m(t) \exp\left[-v \int_0^t \left(\frac{I_\alpha(z)}{n_\alpha} + \frac{I_m(z)}{n_m}\right)dz\right] dt. \tag{17b}$$

Equations (17a) and (17b) give the fractions of the original number of liquid droplets, converted to the respective phases. Therefore, the ratio of the metastable solid phase to the stable solid phase expected in the finally solidified liquid droplets is

$$R = \frac{N_m(t)\Big|_0^\infty}{N_a(t)\Big|_0^\infty}. \qquad (18)$$

In Eq. (18) we assume that none of the particles converted to the metastable phase is retransformed back to the stable α phase.

C. Thermal History of Cooling Liquid Droplets

Plummer[1] and the writer, as will be shown later, have observed that completely melted alumina particles, when resolidified, show varying degrees of porosity, which allows the assumption that some of the liquid particles while cooling can be considered as hollow spheres. The problem then is determining the cooling history of hollow liquid spheres of internal and external radii of r_0 and r, respectively, which at time $t = 0$ are at a uniform reference temperature, for example T_{m_a}. It was realized that different droplets are heated to different temperatures, but since the analysis was mainly concerned with the cooling rates in the droplets near the solidification temperature, it is sufficient to consider a starting reference temperature and ignore the preceding thermal history.

In proceeding with the heat-transfer analysis of the cooling liquid droplets, a very simplified approach was used and a number of assumptions made regarding the mechanism of heat transfer. The basis of the assumptions is indicated in the calculations made in Appendices III.A and B.

For a small particle of an optically transparent material cooling in the temperature range of interest, it can be shown that radiative heat transfer plays a very minor role and hence can be neglected (Appendix III.A).

A simple heuristic approach can be used to determine the particle's temperature history (see Appendix III.C) if, on being subjected rapidly to ambient conditions, a molten spherical shell experiences resistance to heat loss both by conduction and convection. If in a hollow spherical shell steady-state temperature gradients are rapidly established, then the surface heat flux, q, is given by

$$q = \frac{4\pi r^2 \Delta T}{\frac{r - r_0}{k_L \, r_0/r} + \frac{1}{h_s}} . \tag{19}$$

Here q is the heat lost by the hollow sphere in cal/sec, r is the outer radius of the sphere, r_0 is the inner radius of the sphere, k_L is the thermal conductivity of the liquid, h_s is the surface heat-transfer coefficient, and ΔT is the temperature difference between T_A, the outside ambient temperature, and T_i, the temperature of the inner surface. Equation (19) does not hold as $r_0/r \to 0$.

If T is taken as the mean temperature of the particle, then let $(T - T_A) = a(T_i - T_A)$, where a is a constant less than unity. We can then describe the cooling of the particle as

$$-mC_p \frac{dT}{dt} = \frac{\text{heat removed}}{\text{sec} - {}^\circ\text{C}} \times \text{temperature difference forcing heat removal.} \tag{20}$$

If T_A is a function of time, $T_A(t)$, we can combine Eqs. (19) and (20) and get

$$\frac{4 \pi r^3}{3} \rho_a C_p \frac{dT}{dt} = \frac{-4\pi r^2 [T - T_A(t)]}{a\left[\frac{r - r_0}{k_L \, r_0/r} + \frac{1}{h_s}\right]} . \tag{21}$$

here m is the mass of the particle, ρ_a is the particle density, and C_p is the specific heat of the particle. Putting

$$\frac{3}{a \, C_p \, \rho_a r \left[\frac{r - r_0}{k_L \, r_0/r} + \frac{1}{h_s}\right]} = \frac{C_1}{f(\rho_a, r)} = \lambda , \tag{21a}$$

where

$$C_1 = \frac{3}{a\,C_p}, \qquad \text{and} \qquad f(\rho_a, r) = \rho_a r\left[\frac{r - r_0}{k_L\, r_0/r} + \frac{1}{h_s}\right],$$

we have

$$\frac{dT}{dt} + \lambda T - \lambda T_A(t) = 0 . \tag{22}$$

Imposing the initial condition $T = T_m$ at $t = 0$, where T_m is a reference temperature, we have the solution

$$T\, e^{\lambda t}\Big|_{T_m}^{T} = \lambda \int_0^t e^{\lambda t'}\, T_A(t')\, dt'$$

$$T = T_m e^{-\lambda t} + \lambda\, e^{-\lambda t} \int_0^t e^{\lambda t'}\, T_A(t')\, dt' . \tag{23}$$

If $T_A(t)$ is of the form $T_1 + T_2 e^{-bt}$, where T_2 may be either negative or positive indicating a falling or rising ambient temperature, respectively, we have the solution

$$T = T_m e^{-\lambda t} + T_1 (1 - e^{-\lambda t}) + \frac{T_2\, \lambda}{\lambda - b}(e^{-bt} - e^{-\lambda t}) . \tag{23a}$$

Expanding $e^{-\lambda t}$ and neglecting cubes and higher powers of λt, we get

$$T = T_m - \left\{(T_m - T_1)\left(1 - \frac{\lambda t}{2}\right) - T_2\left[1 - \frac{(\lambda + b)}{2}\, t\right]\right\}\lambda t . \tag{24}$$

If the term in the brackets, which is a function of t, can be replaced by a mean value, we can set this term equal to B, where

$$B = \left\{(T_m - T_1)\left(1 - \frac{\lambda \bar{t}}{2}\right) - T_2\left[1 - \frac{(\lambda + b)}{2}\, \bar{t}\right]\right\}$$

in which $\bar{t}$ is a mean time. Thus we have

$$T = T_m - B\, \lambda\, t . \tag{25}$$

D. The Ratio R, of Metastable to Stable α Phase

Equation (25) describes approximately the temperature of a hollow liquid particle cooling in a changing ambient temperature. It is valid until stable nuclei of a solid crystalline phase begin to appear and grow. Thereafter, the temperature history becomes complicated,

because of the release of the heat of fusion. This also implies that the nucleation-rate ratio $I_m(T)/I_a(T)$ at a particular temperature, T (in Fig. 2a), is stabilized momentarily. Hence, there is greater likelihood of the liquid drop being converted completely into the crystalline phase, whose nuclei appear first.

We can now rewrite Eq. (18) as

$$R = \frac{n_a}{n_m} \frac{\int_0^\infty I_m(t) \exp\left[-v \int_0^t \left(\frac{I_a(z)}{n_a} + \frac{I_m(z)}{n_m}\right) dz\right] dt}{\int_0^\infty I_a(t) \exp\left[-v \int_0^t \left(\frac{I_a(z)}{n_a} + \frac{I_m(z)}{n_m}\right) dz\right] dt}, \qquad (26)$$

where $I_a(t)$ and $I_m(t)$ are given from Eq. (1). Rewriting these expressions and substituting T as a function of time, we get

$$I_a(t) = C_v \exp\left[\frac{-16\pi\sigma_a^3 T_{m_a}^2}{3k(T_{m_a} - B\lambda t)(B\lambda t)^2 \Delta H_{f_a}^2} - \frac{E_n}{k(T_{m_a} - B\lambda t)}\right],$$

where $C_v = n n_s^* \frac{kT}{h}$ is taken as constant and $T = T_{m_a} - B\lambda t$ from Eq. (25). Putting $B\lambda t = y$, we get

$$I_a(y) = C_v \exp\left[\frac{-16\pi\sigma_a^3 T_{m_a}^2}{3k(T_{m_a} - y)(y)^2 \Delta H_{f_a}^2} - \frac{E_n}{k(T_{m_a} - y)}\right]. \qquad (27a)$$

Making similar changes for I(z) by using $B\lambda z = x$, we get

$$I_a(x) = C_v \exp\left[-\frac{16\pi\sigma_a^3 T_{m_a}^2}{3k(T_{m_a} - x)(x)^2 \Delta H_{f_a}^2} - \frac{E_n}{k(T_{m_a} - x)}\right]. \qquad (27b)$$

Transforming also the variables in $I_m(t)$ and $I_m(z)$, we get

$$I_m(y) = C_v \exp\left[\frac{16\pi\sigma_m^3 T_{m_m}^2}{3k(T_{m_a} - y)(y + T_{m_m} - T_{m_a})^2 \Delta H_{f_m}^2} - \frac{E_n}{k(T_{m_a} - y)}\right] \qquad (27c)$$

$$I_m(x) = C_v \exp\left[\frac{16\pi\sigma_m^3 T_{m_m}^2}{3k(T_{m_a} - x)(x + T_{m_m} - T_{m_a})^2 \Delta H_{f_m}^2} - \frac{E_n}{k(T_{m_a} - x)}\right]. \tag{27d}$$

Re-expressing Eq. (26) in terms of new variables, we get from Eq. (27)

$$R = \frac{n_a}{n_m} \frac{\int_0^\infty I_m(y) \exp\left\{-\frac{v}{n_a B\lambda} \int_0^y \left[I_a(x) + \frac{n_a}{n_m} I_m(x)\right] dx\right\} dy}{\int_0^\infty I_a(y) \exp\left\{-\frac{v}{n_a B\lambda} \int_0^y \left[I_a(x) + \frac{n_a}{n_m} I_m(x)\right] dx\right\} dy}. \tag{28a}$$

Putting $\frac{v}{n_a B\lambda} = K$, we get

$$R = \frac{n_a}{n_m} \frac{\int_0^\infty I_m(y) \exp\left\{-K \int_0^y \left[I_a(x) + \frac{n_a}{n_m} I_m(x)\right] dx\right\} dy}{\int_0^\infty I_a(y) \exp\left\{-K \int_0^y \left[I_a(x) + \frac{n_a}{n_m} I_m(x)\right] dx\right\} dy}. \tag{28b}$$

Equation (28) shows that, provided n_a/n_m can be assumed constant, the ratio R of metastable to stable phase in the solidified spherical particles is a function of the parameter K, the various terms of which have been defined in Eqs. (3), (21a), and (25).

The right side of Eq. (28) has three different unknown constants σ_a, σ_m, and T_{m_m}. Absence of measured values of these constants prevent determination of a theoretical curve of R vs K, against which the experimental data might be compared. However, some of the aspects of its behavior can be seen in Fig. 3.

Figure 3a is a plot of the nucleation rate I vs the variable y or x, which are equivalent. Figure 3b shows the multiplying function

$$F = \exp\left\{-K \int_0^y \left[I_a(x) + \frac{n_a}{n_m} I_m(x)\right] dx\right\}$$

for different values of K, the quench rate-determining parameter. Figure 3c and d show the products $I_m F$ and $I_a F$, respectively. The

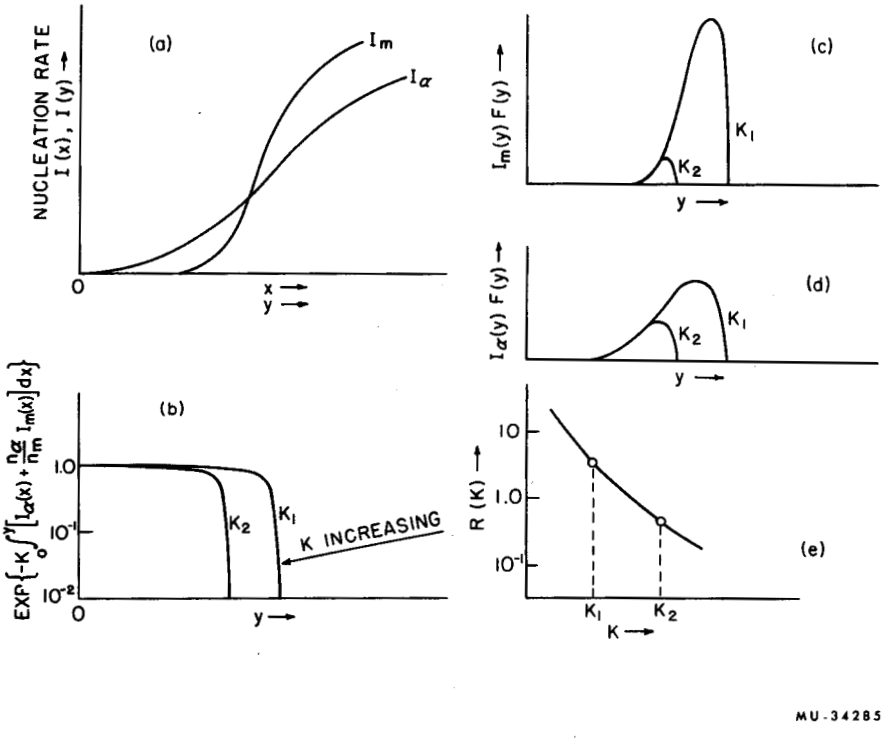

Fig. 3. Plots of (a) nucleation rates I_m and I_α vs variables x and y; (b) the exponential integral in Eq. (28) vs y for different values of k, the quench rate-determining parameter; (c) the integrand of numerator in Eq. (28); (d) the integrand of denominator in Eq. (28); and (e) the ratio R of metastable to stable α phase vs the quench-rate parameter K.

areas under the curves give the numerator and denominator of Eq. (28). Figure 3e gives a plot of R vs the quench-rate-determining parameter, K. Since we have $K = v/n_a B\lambda$, as the cooling rate decreases, $B\lambda$ decreases. This increases K and decreases R, the ratio of metastable to stable α phase. Therefore, increasing the quenching rate of a hollow spherical liquid particle increases the probability of the metastable crystalline phase being formed.

III. EXPERIMENTAL PROCEDURE

A. Feed-Material Preparation

In experiment I, commercial sapphire boules were crushed either in a jaw crusher or by hand in a steel mortar into coarse size fractions. The accumulated iron was separated magnetically. A second set of experiments, designated experiment II, was conducted after an earlier report on this investigation was published.[15] In the latter, the possibility of iron contamination was eliminated by reducing the boules into coarse size fractions by heating to $\simeq$ 1000°C in a furnace, then quenching in cold water. This shattered the 2-1/2-in. by 3/4-in.diam boules into coarse particles with diameters of a few millimeters. Final reduction in both experiments was carried out in an alumina-lined ball mill using alumina balls.

The crushed powder was separated into different-sized fractions by the use of standard sieves in the size ranges 37 to 44μ, 44 to 53μ, 53 to 61μ, 61 to 74μ, 74 to 88μ, 88 to 104μ, and 104 to 124μ. To handle sizes below 37μ, a commercial air-elutriation device was used.[16]

B. Particle Melting

A commercial direct-current-arc plasma jet was used to melt and spheroidize the particles.[17, 18] The sized particles were fed through a screw feeder and carried by a gas into the jet nozzle (Fig. 4). Several collection-chamber arrangements were used to control the cooling rate of the particles. Experiment I (Fig. 4a) and experiment II (Fig. 4c) were conducted to obtain quantitative data. A third experiment (Fig. 4b) was conducted to obtain qualitative indications of changes in quenching rates. Table I gives the operating conditions of experiments I and II, respectively. Mixtures of argon and hydrogen were used as the plasma gas. Only argon was used for the particle-carrier gas.

In experiment I (Fig. 4a), the ambient temperature was not estimated. In experiment II, temperatures were measured with thermocouples at points P, Q, and R (Fig. 4c) with and without the quench-gas jet operating. Without the quench gas, the experimental conditions are

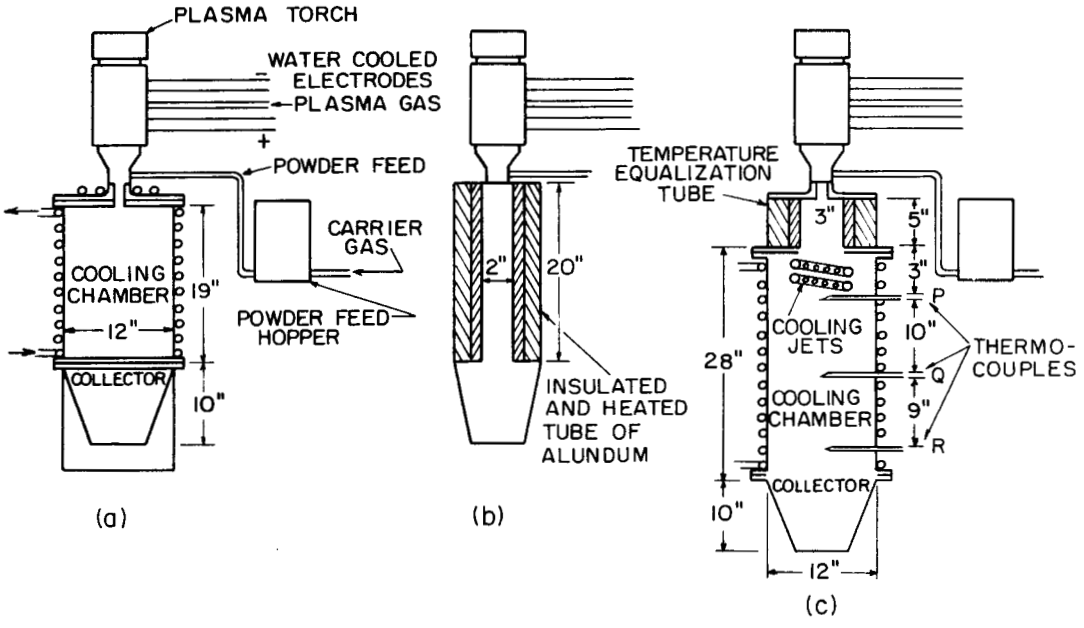

Fig. 4. Diagram of plasma torch and particle-feeding device with three arrangements of quenching and collection chambers. Arrangement (a) represents a moderate quench rate, (b) the slowest quench rate, and (c) with cooling jets at right angles to the path of particle motion, the fastest quench rate.

Table I. Plasma-jet operating conditions for particle spheroidization.

Experiment number	Feed-particle size range (microns)	Operating voltage (V)	Power (kW)	Total argon flow (cu ft/h at STP)	Volume of hydrogen in torch gas (%)
I	37 to 44	30	18.6	25 to 35	10
	53 to 61				
	61 to 74				
	88 to 104				
II	44 to 53	40	16	40	30
	53 to 61				
	61 to 74				
	74 to 88				
	88 to 104				
	104 to 124				

similar to experiment I with the exception that experiment II has a 5-in.-long temperature-equalization tube. The quench-gas jet was estimated to be feeding approximately 400 cu ft/h of room-temperature air, or approximately eight times the volume of gases fed into the plasma jet.

In experiment I, spheroidized material resulting from each feed-size group (Table I) was separately analyzed. In experiment II, though the particle-size fractions were fed separately, no separate collection was made, and they were analyzed as one batch.

C. Particle Collection and Recovery

In all runs a fraction of the particles were not spheroidized. The spheroidized material from any particular size feed always had a considerably wider size distribution than the feed. This could arise from both bubble formation and from the particle shape encountered in the feed material. Considering the initial feed-particle size and the final spheroidized size and apparent density, it was estimated that agglomeration of the feed particles was negligible. Different techniques were used to separate and collect only the spheroidized particles that resulted from the solidification of completely melted feed particles.

The unmelted and partially melted particles from experiment I were removed by allowing the spherical particles to roll down a vibrated inclined polished metal surface. For particles less than 37μ, such separation is not practical and the fraction of unspheroidized particles was estimated by microscopic examination and assumed to be all α alumina. After separation of nonspherical particles, the spheres were divided into size fractions by screening. Subsequently each individual size range was subjected to air elutriation, which further divided them on the basis of their apparent density. The densities were estimated by pycnometric techniques.

In experiment II all spheroidized particles were separated first by using a heavy liquid,[19] s-tetrabromoethane with a density of 2.92. Separation was done in small 15-cc centrifuge tubes and the lighter fraction with a density below 2.92 was collected by decantation. This directly removed the unmelted fractions and yielded completely melted

particles. The spherical particles ($1.62 < \rho_a < 2.92$) were further divided into several density groups by using mixtures of s-tetrabromoethane and CCl_4 ($\rho = 1.62$). Particles in the density range between 1.62 and 1.0 were obtained using CCl_4 and water. Densities of liquid mixtures were directly measured by a pycnometer.

Particles of different sizes from each density fraction were further separated into size fractions by screening. To further eliminate nonspherical particles before x-ray analysis, each final sample was rolled on an inclined polished metal plate as in experiment I.

D. X-Ray-Diffraction Analysis

X-ray powder diffraction using CuK_α radiation was utilized for both phase identification and semiquantitative analysis of the volume fraction of phases present. In experiment I, the amount of two metastable phases γ and δ was collectively reported in the analysis. In experiment II, with more careful analysis, it was possible to separate the γ and δ phases and detect the presence of θ. In order to maintain consistency and a basis of comparison between the two experiments, the total volume of the γ and δ phases was reported. The total area under six x-ray diffraction lines for the metastable phases was compared to the area under selected α alumina lines, depending on the α content of the sample (Table II).

In preparing samples for x-ray analysis, the sample of spherical particles was finely crushed in a small agate mortar. To avoid orientation effects, particularly observable with finely divided α-phase particles, the finely crushed powder was dropped onto a glass slide coated with a plastic varnish. Samples of 2- by 1-cm area and sufficient thickness for quantitative x-ray diffraction were prepared.

The ratio, R_A, of the areas of the metastable to stable α-phase lines was related to R, the absolute ratio of volume of metastable phases to the stable α phase by a standardization procedure in the following manner. Let $1/R = r$ = the true ratio of α/m in the unknown sample, and $r_A = \Sigma \alpha_i / \Sigma m_j$, the ratio of the sum of the areas of i, α lines and j, m lines selected for comparison in any sample. If we add

Table II. X-ray-diffraction lines used in semiquantitative analysis of phases present in quenched alumina spheres

α phase		Metastable phases		
> 90 volume % "d" spacing (Å)	< 90 volume % "d" spacing (Å)	Phase	"d" spacing (Å)	
1.099	2.552	δ	2.59	
1.078	2.089	δ	2.46	
0.998	1.601	δ	2.277	combined area
		γ	2.288	
		δ	1.989	combined area
		δ	1.980	

a volume fraction v of known α-phase material and determine r_A for this sample, then it can be shown that $r_A = k\,[r(1+v) + v]$, where k may be taken as a constant.

A plot of r_A vs v can be made, and if the assumption of linear relationship is valid, a straight line will be obtained. Then from the slope k of this line, we have

$$r_A\Big|_{v=0} = r_{A_0} = kr = \frac{k}{R}.$$

However because we have $R_A = 1/r_{A_0}$, it follows that

$$R = \frac{k}{r_{A_0}} = kR_A.$$

The value of k was determined for both sets of α lines in Table II and average values $k_1 = 0.22$ and $k_2 = 1.53$ were obtained for the >90% α and <90% α, respectively, by using same set of m-phase lines in both cases.

E. Microscopic Analysis

Direct microscopic observation of the spheroidized material was made by mixing the spherical particles with powdered glass having the same thermal-expansion coefficient and hot pressing (below 650°C) the mixture in vacuum to obtain a dense, polishable, and etchable composite. Polished sections of specimens were examined directly and also after etching with orthophosphoric acid at 185 to 195°C for about 10 min. For metallographic examination in all cases, a thin gold layer was vapor-plated on the surface prior to examination, in order to decrease internal reflections. Thin sections of selected samples were prepared for examination of optical properties under the petrographic microscope. Replicas of etched surfaces were made for examination under the electron microscope, to obtain information on surface characteristics such as grain boundaries.

F. Other Analyses

In order to observe the transformation characteristics of the metastable phases on heating, differential thermal analysis was made on spheroidized material which by x-ray examination was found to have more than 80% of the metastable phases. This same material was heated to various temperatures for extended periods to determine weight and phase changes.

Infrared analysis was made by the potassium bromide pelletizing technique, between 2 and 15μ to indicate the presence of hydroxyl ions. Infrared absorption curves were obtained for the feed material, spheroidized material containing a high fraction of metastable phases, and γ-alumina formed by dehydrating aluminum monohydrate.

A high-speed movie camera was used to determine the average velocity of particles when they emerged from the plasma-flame region. A speed of 6000 frames/sec was used, and the velocity was determined by measuring the length of the streak caused by an individual particle during the exposure time of one frame (Fig. 5).

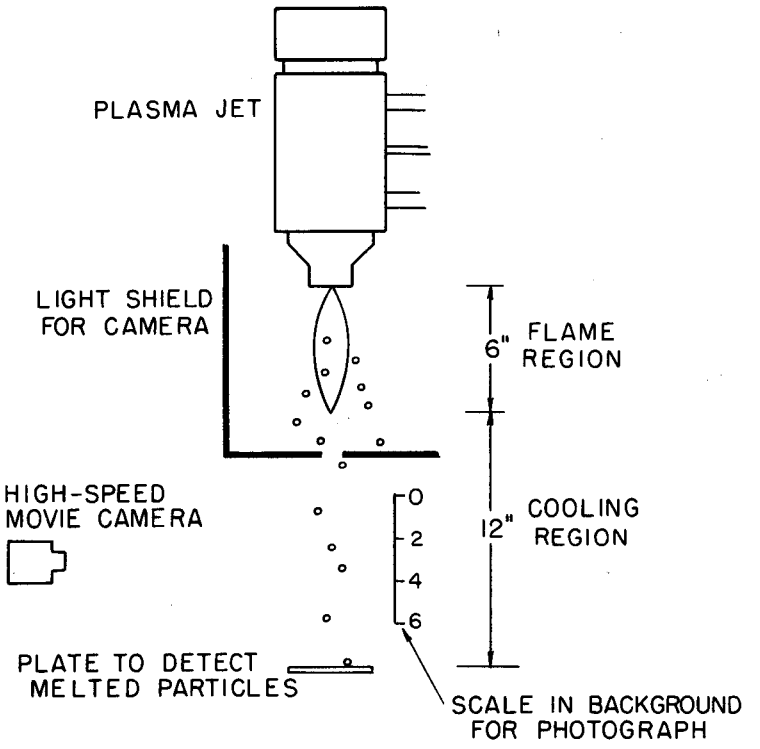

Fig. 5. Diagram showing arrangement for particle-velocity and solidification-distance measurement.

IV. EXPERIMENTAL RESULTS

A. Ambient Temperatures During Particle Cooling

In experiment I (Fig. 4a), the cooling liquid droplets in their vertical downward movement were subjected to a decreasing ambient temperature condition. The particles of larger initial momenta which traveled a greater distance before solidification experienced a lower average ambient temperature than those with smaller initial momenta. If T_A, the ambient temperature in Eq. (23), is taken as a decreasing function of time of the general form $T_A(t) = T_1 + T_2 e^{-b_1 t}$, then the term B in Eq. (25) is given by

$$B_I = \left\{ (T_m - T_1) \left(1 - \frac{\lambda_I \bar{t}}{2} \right) - T_2 \left[1 - \frac{(\lambda_I + b_1)\bar{t}}{2} \right] \right\}, \qquad (29)$$

where $1/\lambda = f(\rho_a, r)/C_1$ from Eq. (21a), and b can be taken as directly proportional to λ. Then B_I increases as $1/\lambda$ increases, since T_m is greater than $T_1 + T_2$.

To reduce this variation in T_A, we undertook experiment II with cooling jets and a temperature equalization chamber. Thermocouple readings at points P, Q, and R (Fig. 4c) indicate the effect of the modification (Table III).

Although no temperature readings were taken at levels higher than P, final analysis of the particles indicates that particles with smaller momenta, completing their solidification above the point P, experience an average ambient temperature substantially lower than that at point P because of the injection of a large volume of cold air. Therefore, for all particles if we postulate a different form of the time-dependent ambient temperature $T_A(t) = T_3 - T_4 e^{-b_2 t}$ --a somewhat rising ambient temperature until about point P, after which it remains constant--then B is given by

$$B_{II} = \left\{ (T_m - T_3) \left(1 - \frac{\lambda_{II} \bar{t}}{2} \right) + T_4 \left[1 - \frac{(\lambda_{II} + b_2)\bar{t}}{2} \right] \right\}, \qquad (30)$$

which decreases as $1/\lambda$ increases, since T_m is greater than $T_3 - T_4$.

Table III. Average temperature in °C in cooling chamber of experiment II

	P	Q	R
Without air jets	1200	450	275
With air jets	420	300	250

B. Bubble Formation and Particle-Density Distribution

In experiment II the yield of melted particles was 64% of the feed material input. The losses are due to deposits on extension tube walls, formation of large blobs of melted Al_2O_3 solidifying near the tip of the nozzle because of erratic flow of the feed material, and small amounts carried off to atmosphere with escaping gases. Of the total quantity of particles passing through the plasma jet and collected, the fraction having a density less than 2.92 was 10.5%. The density of the remaining 89.5% was between 2.92 to 4.00. A total weight of 35.4 g having density range of 1.00 to 2.92 was analyzed for density distribution.

Figure 6 gives particle-weight distribution vs apparent density for particles of ρ_a less than 2.92. Although no quantitative estimate was made for experiment I, the latter contained a larger percentage of hollow particles than those resulting from experiment II. Density measurements and direct microscopic examination of particles in the 7 to 14μ range showed a remarkable absence of hollow spheres. Also, some large partially melted particles showed fine bubbles in the melted regions. Melting with a pure argon atmosphere also produces bubbles. The liquid-solid change in volume at equilibrium melting temperature of liquid alumina,[20] which has been reported to be 22%, cannot account for the observed bubbles. These observations indicate that the bubble-forming tendency decreased with a faster cooling rate, and the gases causing the bubbles originated inside the liquid mass.

The separation of spherical particles according to their apparent densities was more efficient in experiment II, where heavy liquids were

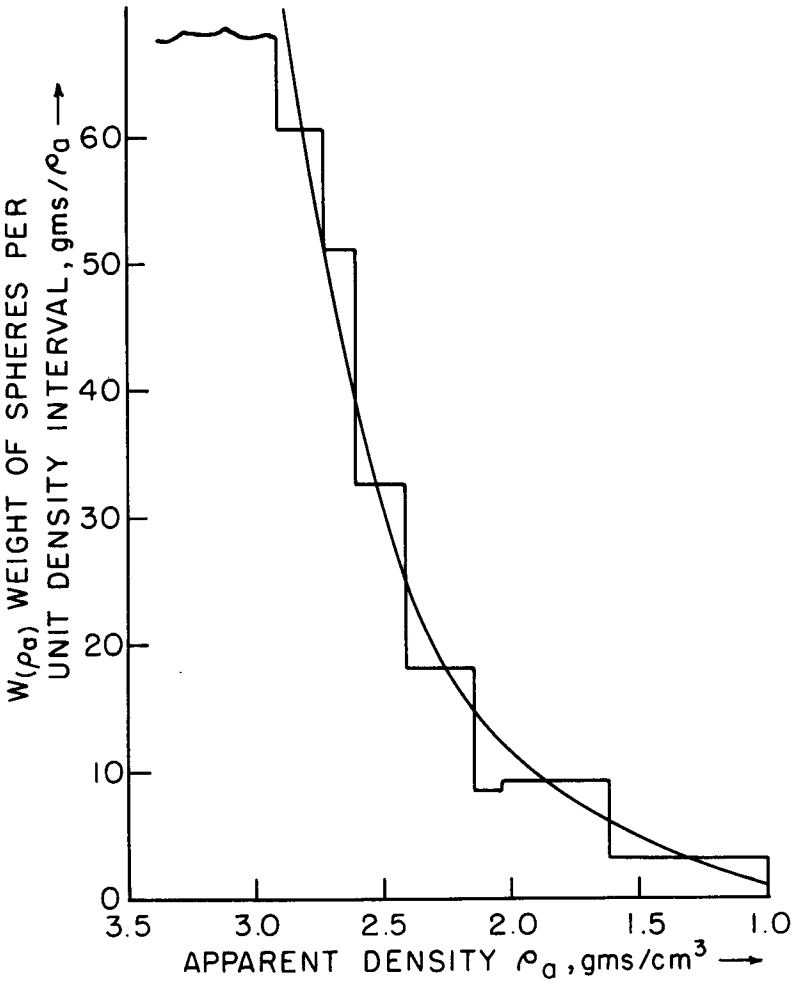

Fig. 6. Plot of weight of spheres per unit density interval vs apparent density in experiment II.

used, than in experiment I, where the air elutriator was employed (see Fig. 7). Figure 7 shows particles of different sizes and densities from those of experiment II.

C. X-Ray Analysis

Figure 8 shows typical x-ray diffractograms for high, medium, and low values of R. Figure 8a shows γ lines agreeing with those obtained by Stumpf[6] and δ lines similar to those identified by Rooksby,[21] along with weak α lines. Figure 8c shows strong δ lines, comparatively weaker γ lines and θ lines similar to those tabulated in reference 6. The θ phase was not mentioned in an earlier report of this investigation.[15]

Tables IV and V and Figs. 9 and 10 show tabulated values and plots of ln R vs ρ_a, respectively, for experiments I and II. The dashed lines are estimated curves corresponding to a single particle-size range. A run made under particle-collection conditions illustrated in Fig. 4b and using the same plasma-jet conditions as experiment I showed lower values of R for a given particle size and density, compared with experiments I and II.

D. Microscopic Analysis

Figure 11 shows results of etching spheroidized Al_2O_3. The unattacked particles correspond to the α phase, and the metastable phases appear attacked by the etchant. The ratios R of metastable to stable phases, obtained by x-ray analysis for a particular sample, correspond to microscopic observation quite closely. Except in rare cases, it was noticed that a particular particle has only one kind of etch, implying complete conversion to one phase.

Thin sections of samples with low and high R were investigated at different angles θ on the petrographic microscope under crossed Nicol prisms. With low R or high α, most particles change color uniformly, indicating single crystals. Few are seen to have more than one grain. With a large percentage of metastable phases, the particles show no change of color, since the metastable phases are more isotropic.

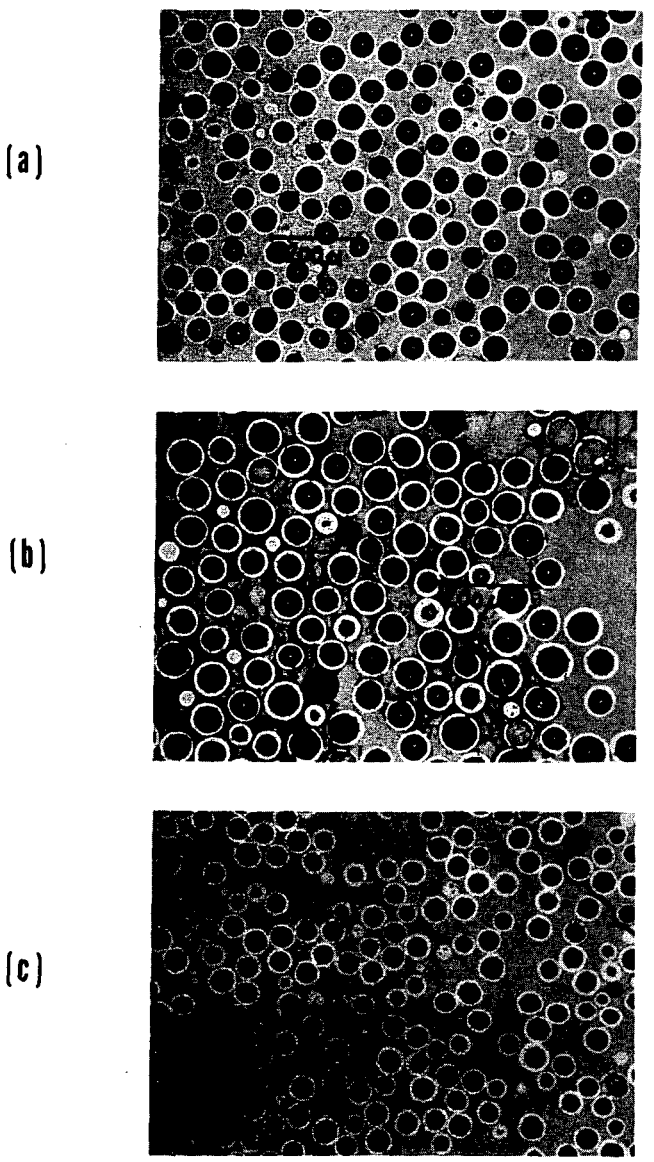

Fig. 7. Polished sections of spherical particles of various sizes and apparent densities embedded in a glass matrix. The dark circles are hollows and the lighter rims are the shells. Variations in the shell thickness in a particular picture and also the appearance of solid-looking particles are due to the spheres being sectioned at different levels.

	Diam (microns)	Density (g/cm^3)
(a)	53-61	1.00-1.62
(b)	74-88	1.62-2.03
(c)	53-61	2.03-2.15

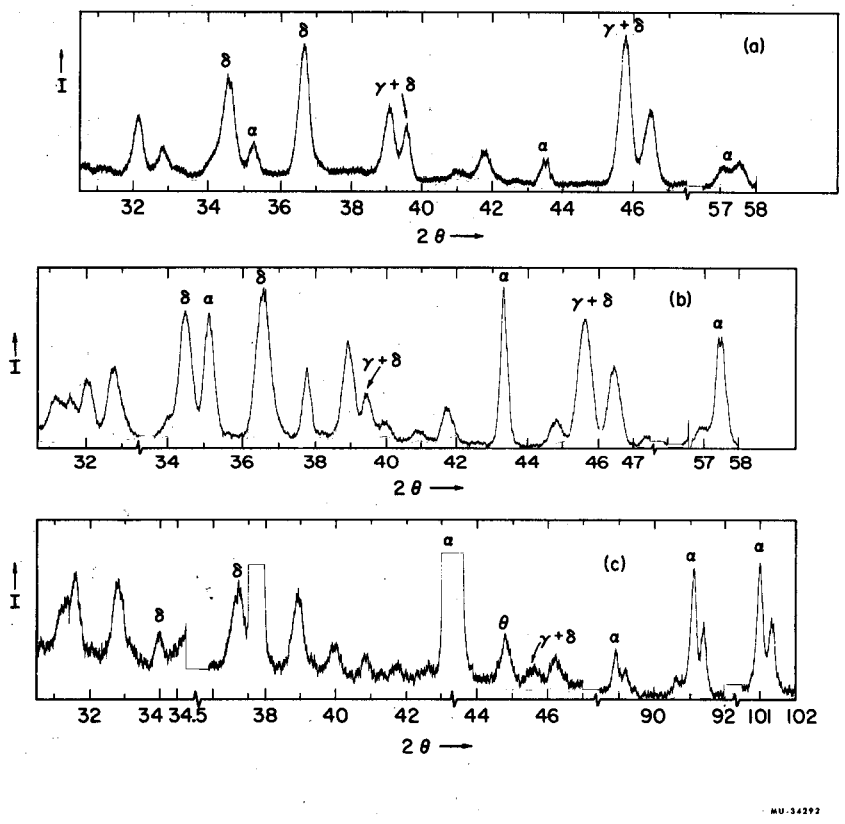

Fig. 8. Typical x-ray diffractograms of three samples of high, medium, and low values of R, respectively, from experiment II.

	Diam (microns)	Density (g/cm^3)	Ln R
(a)	44 - 53	2.61-2.74	3.01
(b)	88-104	2.61-2.74	1.54
(c)	124-147	2.61-2.74	-2.40

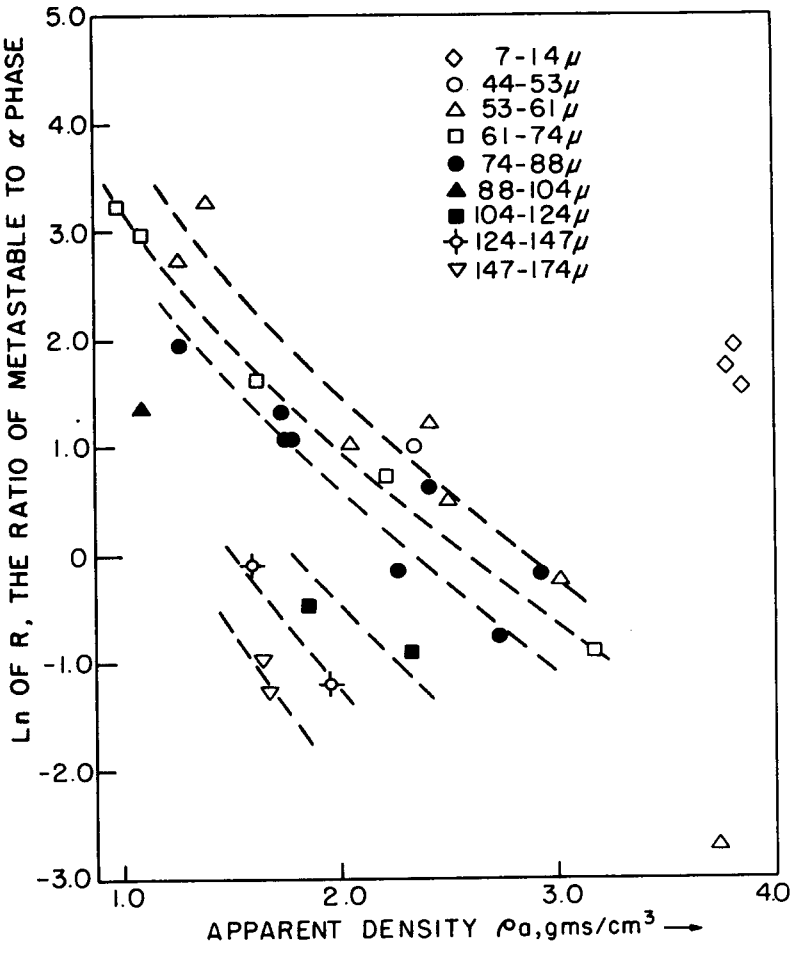

Fig. 9. Ln of R, the ratio of metastable to stable α phase vs apparent density in experiment I with a slow quench rate.

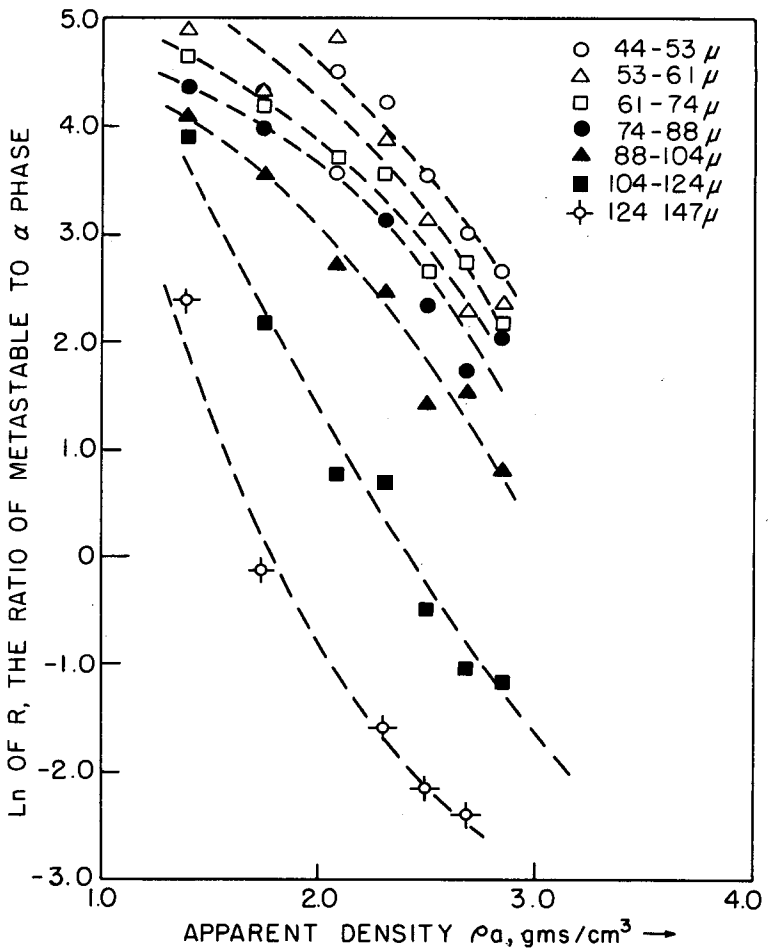

Fig. 10. Ln of R, the ratio of metastable to stable α phase vs apparent density in experiment II with a fast quench rate.

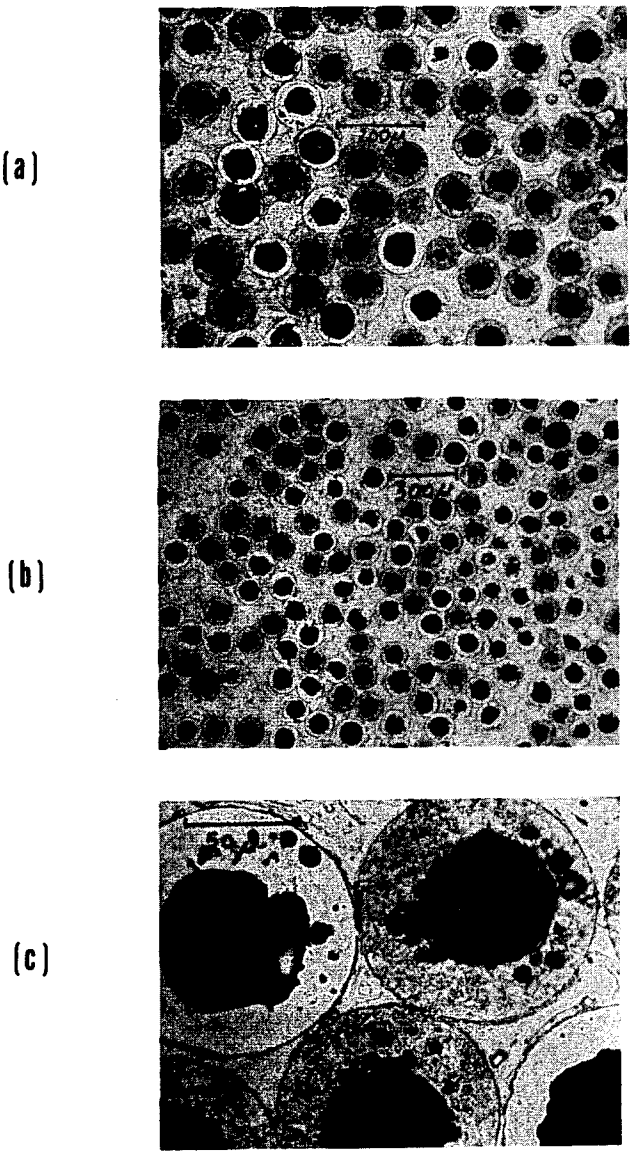

Fig. 11. Polished and etched sections of particles of various sizes and apparent densities embedded in a glass matrix. The relatively lighter spheres are unattacked by the etchant and are of the α phase. The darker spheres which are attacked are the metastable phases.

	Diam (microns)	Density (g/cm^3)	R (from x-ray)
(a)	88-104	2.61-2.74	4.65
(b)	104-124	2.61-2.74	2.25
(c)	Higher magnification of (a).		

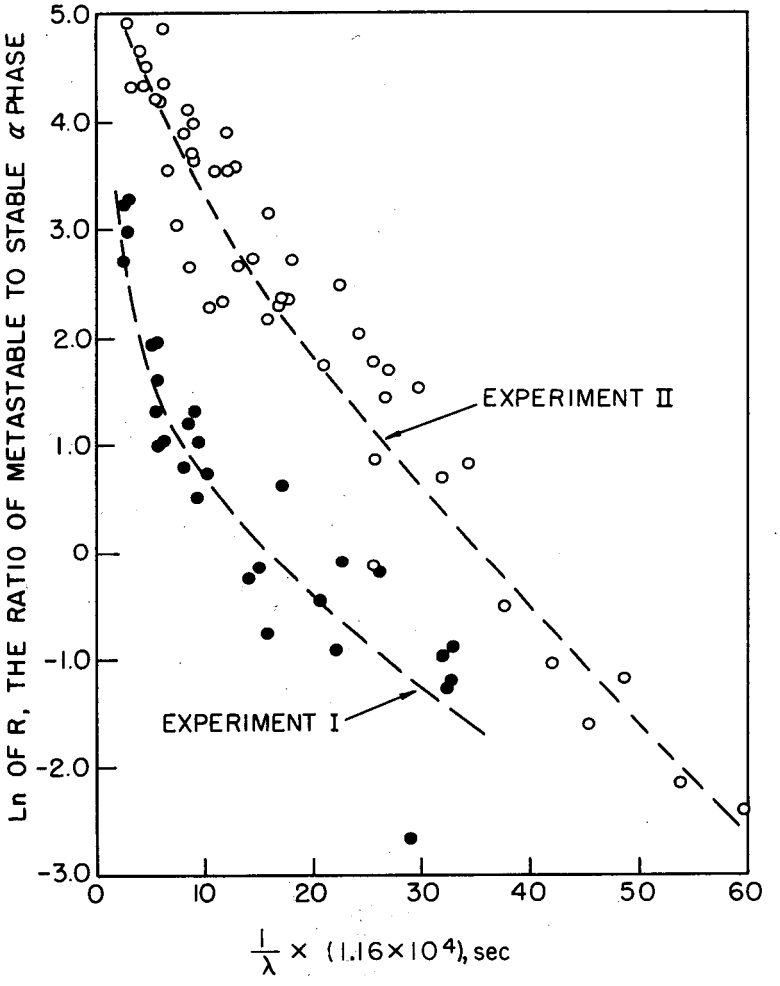

Fig. 12. Ln of R, the ratio of metastable to stable α phase vs the quench rate parameter $1/\lambda$.

Table IV. Logarithm of the ratio of the volume of $\gamma + \delta$ phases to the α-phase volume for different diameters and densities of particles in experiment I.

Average diameter (microns)	Average density (g/cm^3)	ln R	Average diameter (microns)	Average density (g/cm^3)	ln R
7.5	3.77	1.93	67	3.16	-0.92
12.5	3.73	1.74	81	1.26	1.94
14	3.85	1.55	81	1.72	1.31
41	2.87	0.62	81	1.76	1.04
48	2.35	1.00	81	1.78	1.04
57	1.26	2.73	81	2.26	-0.15
57	1.39	3.26	81	2.42	0.62
57	2.04	1.01	81	2.74	-0.76
57	2.42	1.20	81	2.92	-0.18
57	2.49	0.50	96	1.08	1.34
57	3.01	-0.25	114	1.86	-0.48
57	3.72	-2.70	114	2.23	-0.91
67	0.99	3.22	136	1.60	-0.1
67	1.08	2.98	136	1.96	-1.2
67	1.62	1.61	161	1.63	-0.99
67	2.24	0.74	161	1.64	-1.27

Table V. Logarithm of ratio of the volume of the $\gamma + \delta$ phases to the α-phase volume for different diameter and density ranges of particles in experiment II.

Diameter range (microns)		44-53	53-61	61-74	74-88	88-104	104-124	124-147
Average diameter (microns)		48	57	67	81	96	114	136
Density range (g/cm^3)	Average density (g/cm^3)	ln R						
1.00-1.62	1.38		4.90	4.65	4.36	4.10	3.90	2.37
1.62-2.03	1.72	4.31	4.32	4.17	3.98	3.55	2.16	-0.14
2.03-2.15	2.09	4.50	4.85	3.70	3.57	2.71	0.77	
2.15-2.42	2.30	4.21	3.88	3.54	3.14	2.47	0.70	-1.60
2.42-2.61	2.52	3.55	3.11	2.65	2.33	1.43	-0.50	-2.15
2.61-2.74	2.68	3.01	2.28	2.72	1.74	1.54	-1.04	-2.40
2.74-2.92	2.84	2.65	2.35	2.27	2.02	0.81	-1.18	

Although some kind of a substructure is noticeable in Fig. 11c in the etched particles, examination of replicas with the electron microscope revealed no sign of grain boundaries. The pattern observed is attributable to the characteristic etchant attack on the metastable phase. Although the evidence regarding the grain characteristics of the metastable-phase particles is inconclusive, they may be thought to consist of large grains or single crystals, similar to particles of the α-phase material.

E. Results of Other Analyses

Differential thermal analysis of samples containing over 80% of metastable phases gave one exothermic peak starting at 1130°C, the reaction being completed by 1200°C. This agrees with the reported transformation range for the conversion of metastable phases formed by dehydration of hydroxides to alpha alumina in the absence of stabilizing impurities.[6] Heating samples with large amounts of metastable phases for 18 h at 800°C did not change the x-ray diffraction patterns or indicate any loss in weight. Heating to 1200°C showed less than 0.005% loss in weight with complete conversion to alpha alumina. This loss may be considered insignificant.

Infrared absorption spectra of a sample containing a large fraction of metastable phases (primarily gamma) with one exception gave essentially the same spectra as gamma alumina prepared by heating alpha monohydrate to 825°C for 2 h. A strong OH absorption band at 2.9μ present in the dehydrated monohydrate was missing in the plasma formed metastable phase.

The velocity of particles approximately 60μ in diam, as measured by a high-speed movie camera approximately 12 in. from the jet, was of the order of 500 ft/sec.

V. DISCUSSION OF RESULTS

Equation (28) and Fig. 3e predict that R decreases with an increase in the quench rate-determining parameter, $K = v/n_a B\lambda$, where the terms have been defined in Eqs. (3), (21a), and (25). Figures 9 and 10 show that (a) increasing particle size, (b) increasing particle density, or (c) decreasing B, all of which increase K, result in a decrease in R.

Further, if the heat transfer analysis resulting in Eq. (24) is valid and Eq. (28) represents the solidification phenomenon correctly, then a plot of R vs $1/\lambda$ should correlate all points of different particle sizes and densities in any one experiment into one continuous band if B and v/n_a can be assumed constant. Appendix III.B gives a numerical estimate of $1/\lambda$. Also a plot of R vs K should correlate all points of different experiments with different B values into one single band. The dashed lines in Fig. 12 show estimated plots of ln R vs $1/\lambda$ for both experiments. Since the mean value of B_{II} is greater than the mean value of B_I, the band for experiment II fell higher than that of experiment I. If B in each experiment was a constant, then a plot of ln R vs K would combine both curves in Fig. 12 into a single plot.

However, it was shown in Eqs. (29) and (30) that B cannot be taken as a constant. Therefore, for a given value of $R = R_0$, we have $K = K_0$, a constant; and

$$\frac{\lambda_I}{\lambda_{II}} = \frac{B_{II}}{B_I},$$

where $1/\lambda_I$ and $1/\lambda_{II}$ are the abscissae of points where any $\ln R = \ln R_0$ intersects two curves in Fig. 12. But the ratio of B_{II} to B_I is

$$\frac{B_{II}}{B_I} = \frac{\left\{(T_m - T_3)\left(1 - \frac{\lambda_{II}\bar{t}}{2}\right) + T_4\left[1 - \frac{(\lambda_{II} + b_2)\bar{t}}{2}\right]\right\}}{\left\{(T_m - T_1)\left(1 - \frac{\lambda_I\bar{t}}{2}\right) - T_2\left[1 - \frac{(\lambda_I + b_1)\bar{t}}{2}\right]\right\}}, \qquad (31)$$

and the right side of Eq. (31) decreases as $1/\lambda_I$ and $1/\lambda_{II}$ increases.

If we examine Fig. 12 and take two values of R such as $\ln R_1 = 3$ and $\ln R_2 = -1.0$, we see that $B_{II}/B_I = \lambda_I/\lambda_{II}$ corresponding to these

values of R_1 and R_2 goes from 4.5 to 1.7 as predicted by Eq. (31). Therefore, the ambient temperature distributions of the two experiments postulated earlier are most probably of the correct form.

Scatter of the points in the bands in Fig. 12 is attributable to several causes, the most important being (a) the necessity of using size and density ranges instead of specific values, and (b) B not being constant in any experiment.

When droplets of liquid Al_2O_3 are cooled rapidly below their equilibrium melting temperature, increasing cooling rates increases the probability of the droplet being transformed in the order α, θ, δ, and γ. These are crystalline phases of alumina representing an increasing degree of disorder and instability. Consequently, postulation of a pseudo melting temperature for each of the phases θ, δ, and γ is reasonable to explain individual nucleation rate curves (Fig. 2a and b). Observation of the large proportion of single-crystal, spherical α-phase particles supports the assumption that nucleation followed by rapid growth is the mechanism of solidification. Furthermore, particles subjected to similar heating conditions followed by different ambient temperatures during cooling showed similar quench-rate dependence in their ability to convert to the metastable phases during solidification. These evidences suggest, that irrespective of the atomic steps leading to the formation of the first stable nuclei of a particular crystalline phase, the subsequent rapid growth of these nuclei to convert one particle to a single crystalline phase can be considered as the most likely mechanism for solidification of these liquid droplets. The presence of some rare cases, where one single particle converts partially to α phase and partially to a metastable phase, as seen from the microscopic examination of etched particles, is an evidence of the random nature of the nucleation process postulated.

Our findings agree with the general observations of Plummer[1] that (a) the smaller the feed particles of α-alumina, the greater the transformation to metastable phases on rapid quenching of liquid droplets; (b) individual spheres obtained from quenched molten alumina are of a single phase; (c) moderate quenching conditions from the liquid

state accentuate formation of θ- and δ-alumina, whereas faster quench rates lead to larger fractions of the γ phase; and (d) the larger the spherical particle from quenching molten alumina, the less its apparent density. Plummer's objections to considering the cooling rate of molten alumina droplets as the sole criterion for transformation to metastable crystalline phases are based mainly on (a) his observation of a break in the transformation ratio vs radius curve in the neighborhood of 15 to 35μ, and (b) the inability to find mixtures of m- and α-alumina in individual particles. He expected these if the ratio of phases present were a continuous function of cooling rate.

In this investigation a continuous variation of the ratio of the metastable to stable phase vs the quenching rate was found as proposed in the hypothesized mechanism in Eq. (28). Also, if nucleation is followed by rapid growth then individual particles should show only one crystalline phase. Therefore, the two primary objections made by Plummer to the quenching rate being the criterion of primary importance in the solidification mechanism of molten alumina can be countered by the proposed hypothesis of the nucleation kinetics and its relationship to quenching rates.

The absence of weight loss on heating and the observed infrared absorption spectra of the metastable phases rule out hydroxyl stabilization that has been proposed as a mechanism for the formation of similar metastable phases by decomposition of hydrates or other aluminum salts.[22] The purity of feed material minimized the presence of stabilizing impurities.

VI. CONCLUSIONS

When liquid aluminum oxide, in the form of finely divided droplets, is subjected to rapid cooling in a gaseous atmosphere and allowed to solidify, it results in formation of one of the crystalline phases α, θ, δ, or γ. The probability of the formation of any particular phase does not depend on any extraneous factors, but is controlled only by the rate of cooling. Higher rates yield phases of increasing degree of disorder. Homogeneous nucleation of the particular crystalline phase from the supercooled liquid, followed by rapid growth, is proposed as the most likely mechanism for the liquid-solid transformation process. The solidified droplets show various degrees of bubble formation.

ACKNOWLEDGMENTS

The author expresses grateful appreciation to Professor R. M. Fulrath for his counsel and guidance during the course of the work. He is grateful to Professor D. R. Olander for many helpful discussions with regard to the mathematical portion of the work, and to Professor J. A. Pask for his stimulating suggestions.

He wishes to thank Robert Buehrig for preparation of the photomicrographs.

This work was done under the auspices of the U. S. Atomic Energy Commission.

APPENDIX I.

A. Temperature Estimation where Nucleation Rates of Two Phases are Equal

The probability that a temperature T_c in Fig. 2 exists where I_a and I_m cross over can be found as follows. At T_c, we have

$$\frac{I_m(T_c)}{I_a(T_c)} = 1 \quad \text{or} \quad \ln \frac{I_m(T_c)}{I_a(T_c)} = 0 . \tag{32}$$

Substituting the constants for the respective phases in Eq. (1), we have

$$\frac{-16\,\pi\,\sigma_m^3\,T_{m_m}^2}{3kT_c(T_{m_m} - T_c)^2\Delta H_{f_m}^2} + \frac{16\,\pi\,\sigma_a^3\,T_{m_a}^2}{3kT_c(T_{m_a} - T_c)^2\Delta H_{f_a}^2} = 0 ,$$

or

$$\frac{(T_{m_a} - T_c)^2}{(T_{m_m} - T_c)^2} = \left(\frac{\Delta H_{f_m}}{\Delta H_{f_a}}\right)^2 \left(\frac{\sigma_a}{\sigma_m}\right)^3 \left(\frac{T_{m_a}}{T_{m_m}}\right)^2 . \tag{33}$$

Here the subscripts refer to the respective phases, and T_m, ΔH_f, and σ have been defined earlier.

The liquid-crystal interfacial energies, σ, have been estimated directly from the solidification studies of finely dispersed liquid droplets.[3] The nucleation process was inferred to be homogeneous. The gram atomic interfacial energy, σ_g, is related to σ as $\sigma_g = N^{1/3}\,V^{2/3}\,\sigma$, where N is Avogadro's number, and V is the molecular volume. It was shown that σ_g can be directly related to the heat of fusion as

$$\sigma_g = C\,\Delta H_f .$$

The value of C for a large number of metals studied was 0.46. For different classes of materials, such as covalent-bonded metals, ionic liquids, organic liquids, etc., C varied between 0.32 and 0.61.[12b] Taking a constant value of C in relating two different liquid-crystal interfacial energies of the same material, we have

$$\frac{\sigma_a}{\sigma_m} = \frac{\sigma_{g_a}}{\sigma_{g_m}} = \frac{\Delta H_{f_a}}{\Delta H_{f_m}} . \tag{34}$$

Therefore we have from Eqs. (33) and (34)

$$\left(\frac{\Delta H_{f_m}}{\Delta H_{f_a}}\right)^2 \left(\frac{\sigma_a}{\sigma_m}\right)^3 \left(\frac{T_{m_a}}{T_{m_m}}\right)^2 = \left(\frac{\Delta H_{f_a}}{\Delta H_{f_m}}\right)\left(\frac{T_{m_a}}{T_{m_m}}\right)^2 = a\left(\frac{T_{m_a}}{T_{m_m}}\right)^2 \tag{35}$$

where $a = \Delta H_{f_a} / \Delta H_{f_m} > 1$ as estimated from heat-of-solution studies on γ-phase alumina.[23] From Eqs. (33) and (35) we have

$$\frac{T_{m_a} - T_c}{T_{m_m} - T_c} = \sqrt{a}\, \frac{T_{m_a}}{T_{m_m}} ,$$

and therefore,

$$T_c = \frac{(\sqrt{a} - 1) T_{m_a} T_{m_m}}{(\sqrt{a}\, T_{m_a} - T_{m_m})} > 0 .$$

We also get

$$T_{m_m} - T_c = T_{m_m} \frac{(T_{m_a} - T_{m_m})}{(\sqrt{a}\, T_{m_a} - T_{m_m})} > 0 .$$

Thus T_c is a positive real value where $T_c < T_{m_m} < T_{m_a}$ as postulated in Fig. 2.

APPENDIX I.

B. Transient Nucleation

If a liquid is suddenly supercooled to a temperature T below the equilibrium melting temperature, then some time must elapse before the steady-state nucleation rate, I, defined by Eq. (1) is attained. If I_0 is the steady-state rate, then it has been shown by several approaches which lead to the same final form,[13, 14] that

$$I(t) \simeq I_0 \exp\left[-\frac{g^2}{4Dt}\right], \tag{36}$$

where t is the time in seconds, g is the number of atoms in a critical size nucleus, and D is the transport factor that can be approximated by

$$D = n_s^* \frac{kT}{h} \exp\left[-\frac{\Delta F_D}{kT}\right]. \tag{37}$$

In Eq. (37) n_s^* is the number of atoms on the surface of a critical nucleus, and ΔF_D, the activation energy for diffusion in the liquid, may be taken equal to the activation energy for viscous flow in liquid Al_2O_3, 30 kcal/mole.[4]

The radius of the critical nucleus,[24a] r^*, is given by $-2\sigma/\Delta H_v \times T_m/(T_m - T)$, where ΔH_v is the volumetric heat of fusion, ΔH_f is the molar heat of fusion, V is the molar volume of liquid alumina, and T_m is the equilibrium melting temperature of alumina. We take $\sigma_g = C\ \Delta H_f$ (Appendix I.A), $C_{Al_2O_3} = 0.5$, and the average supercooling, $T_m - T = 0.2\ T_m$,[25] so that $T_m/(T_m - T) = 5$. We then have

$$\sigma = \frac{\sigma_g}{N^{1/3}\ V^{2/3}} \qquad \text{(from Appendix I.A)}$$

$$= \frac{0.5\ \Delta H_f}{N^{1/3}\ V^{2/3}} = \frac{0.5\ \Delta H_v\ V}{N^{1/3}\ V^{2/3}},$$

from which we get

$$r^* = 5\left(\frac{V}{N}\right)^{1/3},$$

$$g \simeq \frac{\text{volume of critical size nucleus}}{\text{average volume of ion}} = \frac{4\pi r^{*3}}{3v},$$

and

$$n_s^* \simeq \frac{\text{surface area of a nucleus}}{\text{surface area occupied by an ion on nucleus surface}} = \frac{4\pi r^{*2}}{n_s}.$$

Then from Eq. (36) the characteristic time, t_c, taken by the liquid drop to attain 1/e of steady-state value is given by $t_c = g^2/4D$. Substituting values of g and D, and assuming the average radius of an ion in Al_2O_3 liquid to be 1 Å, we get $v = V/5N$ at 5 ions per molecule, where N is Avogadro's number. We have for the surface area occupied by an ion on the nucleus surface

$$n_s = \pi \times (10^{-8})^2 = \pi \times 10^{-16}.$$

Taking $T = 0.8\ T_m = 1850°K$, we have

$$t_c = \left(\frac{4\pi r^{*3}}{3v}\right)^2 \frac{\pi \times 10^{-16}}{4 \times 4\pi r^{*2}} \times \frac{6.6 \times 10^{-27}}{1.38 \times 10^{-16} \times 1.85 \times 10^3} e^{8.2}$$

$$\simeq 10^{-7} \text{ sec.}$$

Since the time taken for cooling and solidification of a particle is of the order of 10^{-3} sec we can safely neglect the transients.

APPENDIX II.

Estimate of the Growth Rate of a Crystalline Phase in Solidifying Liquid Droplet

The linear growth velocity of a crystal in a liquid is given by[26]

$$G_L = f \frac{kT}{3 \pi a_0^2 \eta} \left[1 - \exp \left(- \frac{\Delta_g}{kT} \right) \right], \tag{38}$$

where we define $f \simeq 1$ (from reference 13); a_0, the interionic spacing $\simeq 1$ Å; η, the viscosity = 0.6 poise;[4] $\Delta_g = \Delta H_f (\Delta T / T_m) = 0.2 \Delta H_f$; $\Delta T = 0.2 T_m$; $T = 1850°K$; and $\Delta H_f = 26$ kcal/mole.[27] Substituting in Eq. (38), we get

$$G_L = \frac{1.35 \times 10^{-16} \times 1.85 \times 10^3 \times 0.15}{3\pi \times 10^{-16} \times 0.6} = 68 \text{ cm/sec.}$$

Now the volumetric growth rate G_V is given by

$$G_V = \frac{dV}{dt} = \frac{dV}{dr} \cdot \frac{dr}{dt} = 4 \pi r^2 G_L ,$$

where $V = 4\pi r^3/3$ and $dr/dt = G_L$.

If G_L is assumed constant, then we have

$$\frac{dV}{dt} = 4 \pi G_L \left(\frac{3}{4\pi} \right)^{2/3} V^{2/3} = C V^{2/3} . \tag{39}$$

By integrating between $V = V_0$ and V, we get the time required for the nucleus to grow to V,

$$t = \frac{3}{C} \left[V^{1/3} - V_0^{1/3} \right] . \tag{40}$$

If V is the volume of a drop of diameter 6×10^{-3} cm, we then get $t \simeq 2 \times 10^{-3}$ sec, a correct order of magnitude.

APPENDIX III.

A. Radiative Heat Transfer

The radiative-heat-transfer rate for a surface at a temperature T radiating into an infinite medium at a temperature T_a is given by

$$Q_R = \epsilon\sigma (T^4 - T_a^4) , \tag{41}$$

where Q_R is the heat removed per unit area of surface per second, ϵ is the emissivity of the surface, and σ is the Stephan-Boltzmann constant.

For small T_a/T, the radiative heat-transfer rate in calories per sec/cm^2 is approximated by

$$Q_R = \epsilon\sigma T^4 . \tag{42}$$

For opaque bodies, ϵ is a surface-dependent property. For nonopaque bodies, however, ϵ has been shown to depend upon the (a) absorption coefficient and (b) thickness of the material.[28] For a thin sheet of material, ϵ is approximated by

$$\epsilon \simeq c\,\mu\,d , \tag{43}$$

where c is a constant equal to 2, μ is the linear absorption coefficient in cm^{-1}, and d is the sheet thickness in cm. Equation (43) applies when the dimensionless thickness μd is less than 0.1. For a spherical particle of diameter d, c has a value near unity.

The convective-heat-transfer rate during cooling is given by

$$Q_c = h_s (T - T_a) , \tag{44}$$

where Q_c is the heat removed per unit area per second, h_s is the convective-heat-transfer coefficient, T is the surface temperature, and T_a is the ambient temperature. For spherical particles cooling in a turbulent atmosphere, h_s is given by[29]

$$\frac{h_s d}{k_f} = 0.37 \left(\frac{d \rho_f v_f}{\mu_f} \right)^{0.6} , \tag{45}$$

where d is the particle diameter, k_f is the thermal conductivity of the fluid, ρ_f is the density of the fluid, v_f is the relative velocity of fluid with respect to particle, and μ_f is the viscosity of the fluid.

For $Q_R << Q_c$, the radiative heat transfer can be neglected, in comparison with the convective heat transfer. This condition may be found by arbitrarily setting

$$Q_R < \frac{Q_c}{100} \tag{46}$$

and determining the value of d from Eq. (46). For this comparison, the theoretically lowest value of $h_s d/k_f = 2$ may be used,[29] so that the least-effective convective cooling condition is compared with the radiative cooling rate. Using $h_s = 2\,k_f/d$ and Eqs. (42) and (46), we write

$$100\,\epsilon\,\sigma\,T^4 < \frac{2\,k_f}{d}\,(T - T_A)\,. \tag{47}$$

Two cases may be considered: (a) ϵ is a surface property alone, and (b) $\epsilon = \mu d$ for spheres of nonopaque materials. Then, we have for (a)

$$d < 2\,k_f\,\frac{(T - T_a)}{100\,\epsilon\,\sigma\,T^4}\,, \tag{48}$$

and for (b)

$$d^2 < \frac{2\,k_f\,(T - T_a)}{100\,\mu\,\sigma\,T^4}\,. \tag{49}$$

We use the values $\sigma = 5.67 \times 10^{-5}$ erg cm^{-2} sec^{-1} deg^{-4}, $T = 2300°K$, $T_a = 700°K$, and $k_f = 1.2 \times 10^{-4}$ cal sec^{-1} cm^{-1} deg^{-1} for air at 700°K. Values of T and T_a are selected for the most favorable radiative cooling condition.

No value is reported for μ, the absorption coefficient for liquid Al_2O_3. However, from estimates based on the crystal transmission coefficient[6] of solid Al_2O_3, a value of $\mu = 0.1$ may be used as a lower limit. An upper limit of $\mu = 1.0$ may be taken arbitrarily if the liquid is considered very much more absorptive to radiation than the crystalline solid. For bulk liquid alumina, $\epsilon = 0.15$ has been reported.[6] Table VI gives the diameter of particle d, below which radiative heat transfer can be neglected on the basis of above assumptions.

Since assumption (a) is not realistic, the particles were assumed transparent, and for the size-range analyzed, radiative heat transfer was neglected.

Table VI. Diameter of liquid particles for which radiative heat transfer may be neglected.

Particle light transmission	μ	ϵ	d (microns)
Opaque		0.15	< 8
Transparent	0.1	< 32	< 320
Transparent	1.0		< 100

APPENDIX III.

B. Comparison of Convective and Conductive Resistances to Cooling of a Hollow Sphere

In the expression for resistivity to heat transfer, Eq. (21), we had assumed earlier[15] that

$$\frac{1}{h_s} << \frac{r}{k_L} \frac{(1 - r_0/r)}{r_0/r} .$$

We also neglected the surface resistance in comparison with the conductive resistance in determining the heat-transfer parameter λ (Eq. 21a). We now outline a procedure for establishing an upper limit on $1/h_s$ on the basis of particle-velocity measurement and the travel distance required to solidify a particle. From this we show that $1/h_s$ could be comparable in value to $r/k_L \times (1 - r_0/r) r/r_0$ for the particle size range under consideration.

It was estimated that particles do not begin to cool until they are at least 6 in. from the jet (Fig. 5). Also, using a glass plate in the particle path, we estimated that all particles with diameters of $\simeq 60\mu$ are solidified within 18 in. The movie films (6000 frames/sec) gave an average velocity of 500 ft/sec, determined by streak-length measurement. Hence 12 in. is an upper limit on the cooling distance.

For the average surface heat-transfer coefficient, we can write

$$\bar{h}_s = \rho_a V \frac{[C_p(T_i - T_s) + \Delta H_v]}{A(\bar{T} - T_A)\, \ell / \bar{v}} . \qquad (50)$$

Here ρ_a is the particle density in g/cm^3, V is the particle volume in cm^3, A is the particle surface area in cm^2, $C_p = 0.31$ is the specific heat of liquid Al_2O_3, $T_i \geq 1.2\ T_m$ (arbitrary estimate) is an unknown temperature to which the particle is heated when it just emerges from the flame, $T_s = 0.8\ T_m$ is the estimated temperature to which the liquid is supercooled,[24] $\Delta H_v = 0.765$ cal/cm^3 is the heat of fusion with a liquid density of $\simeq 3$ g/cc,[20,27] $\bar{T}$ is the mean temperature of a particle during cooling $= (1.2 + 0.8)/2\ T_m = T_m$, $T_A = 1000°C$ is the average ambient temperature the particle experiences while cooling in hot gases, $\ell = 12$ in. is the cooling distance, and $\bar{v} = 500$ ft/sec is the average velocity.

The term $\ell/\bar{v} = t_0$, the time required to complete solidification, is not constant but is some function of ρ_a and r. Also it consists of two parts--t_a, the time to cool from T_i to T_s, and t_b, the time to release the considerably large heat of fusion, so that

$$t_0 = t_a + t_b \,. \tag{51}$$

To obtain the form of t_0, a simplified surface-dependent cooling equation may be written for the particle, assuming a form for h_s given by

$$\frac{h_s d}{k_f} = 0.37 \left(\frac{dv\rho}{\mu}\right)^{0.6} \,. \quad \text{(from Appendix III.A)} \tag{52}$$

If we take $v = C_1/\rho_a r$ in Eq. (52)--a reasonable supposition that smaller particles slow down faster--we have

$$h_s = C_2 \rho_a^{-0.6} r^{-1} \,. \tag{53}$$

Then the cooling equation is

$$\frac{dT}{(T - T_A)} = - \frac{C_3 h_s \, dt}{\rho_a r} \tag{54}$$

and we have the solution

$$\frac{T - T_A}{T_i - T_A} = \exp\left(-C_4 \rho_a^{-1.6} r^{-2}\right) t \,, \tag{55}$$

where the C_i are all constants. Then from Eq. (55), we have

$$t_a = \ln \frac{(T_i - T_A)}{(T_S - T_A)} \times \frac{\rho_a^{1.6} r^2}{C_4}$$

$$= C_5 \rho_a^{1.6} r^2 \,. \tag{56}$$

Similarly, we have

$$t_b = \frac{\rho_a V (\Delta H_v)}{A(T_S - T_A) h_s} = C_6 \rho_a^{1.6} r^2 \,,$$

where we have substituted from Eq. (53) and combined constants, and therefore,

$$t_0 = t_a + t_b = (C_5 + C_6) \rho_a^{1.6} r^2 = C_7 \rho_a^{1.6} r^2 \,. \tag{57}$$

Estimating C_7 from the experimental value of $\ell/\bar{v}$, we have

$$t_0 = \frac{1}{500} = 2 \times 10^{-3} \text{ sec} .$$

Taking $\rho_a = 4$, and $r = 3 \times 10^{-3}$ cm as the room temperature values of the particles, we have

$$C_7 = \frac{2 \times 10^{-3}}{(4)^{1.6} (3 \times 10^{-3})^2} = 24.0 .$$

We now substitute $\ell/\bar{v} = C_7 \rho_a^{1.6} r^2$ in Eq. (50) and get

$$\bar{h}_s = \rho_a^{-0.6} r^{-1} \frac{[0.31 \times 0.4 \times 2313 + 765]}{(2313 - 1273) \times 24}$$

$$= 0.0138 \rho_a^{-0.6} r^{-1} , \qquad (58)$$

which is of the same form as we assumed in Eq. (53).

In the absence of reported values we can estimate k_L, the thermal conductivity of liquid Al_2O_3, on the basis of the value for the solid k_s by using the following arguments. The thermal conductivity[24b] of a material when transformed from solid to a disordered liquid phase is likely to decrease considerably, due to the reduction of the phonon mean free path. Values are likely to be nearer those of glass at lower temperatures. We arbitrarily choose

$$k_L = \frac{1}{3} k_s , \qquad (59)$$

where $k_s = 0.018$ cal/sec cm °C,[6] as the value for a polycrystalline solid at 1800°C.

From Eqs. (58) and (59) we can write for the heat resistivity

$$\left[\frac{r}{k_L} \frac{(1 - r_0/r)}{r_0/r} + \frac{1}{h_s} \right] = 3.33 \times 10^2 \left[\frac{1}{(1 - \rho_a/\rho_t)^{1/3}} - 1 + C \rho_a^{0.6} \right] \qquad (60)$$

where the estimated upper limit of C above is 3/7.

Putting $a = 1$ and substituting from Eq. (60) we can write for $1/\lambda$ in Eq. (21a)

$$\frac{1}{\lambda} = 34.4 \rho_a r^2 \left[\frac{1}{(1 - \rho_a/\rho_t)^{1/3}} - 1 + C \rho_a^{0.6} \right] , \qquad (61)$$

the function used to correlate data in Fig. 12.

APPENDIX III.

C. Comparison of the Analytical Solution for the Determination of Hollow-Particle Temperature History with the Heuristic Solution of the Problem

The general solution of the hollow-sphere cooling problem is given in reference 30, page 246, Eq. (2). Let

$$\theta(t, r) = \frac{T - T_A}{T_m - T_A} . \tag{62}$$

Then the heat-conduction equation is given by

$$\frac{\partial \theta}{\partial t} = \kappa \nabla^2 \theta \tag{63}$$

subject to the initial condition

$$\theta(r, 0) = 1 \tag{64}$$

and the boundary conditions

$$\left(\frac{\partial \theta}{\partial r}\right)_{r=r_i} = 0 \tag{65}$$

and

$$\left(\frac{\partial \theta}{\partial r}\right)_{r=r_0} = - \frac{h_s}{k_L} \theta(r_0, t) \tag{66}$$

where $\kappa = k_L/\rho C_p$ is the diffusion constant, r_i is the inside radius of the shell, and r_0 is the outside radius of the shell. The solution to (63) is given by Eq. (2), reference 30, which is of the form

$$\theta(r,t) = \frac{2}{r} \sum_{n=1}^{\infty} e^{-\kappa a_n^2 t} R_n(r) \int_{r_i}^{r_0} r' R_n(r') dr' , \tag{67}$$

where R_n and a_n have been defined in reference 30.

An average temperature, $\overline{\theta}(t)$, of the particle, can be determined so that

$$\frac{4\pi}{3} (r_0^3 - r_i^3) \overline{\theta}(t) = \int_{r_i}^{r_0} \theta(r, t)\, 4\pi r^2\, dr \tag{68}$$

and $\overline{\theta}(t)$ is of the form

$$\overline{\theta}(t) = \sum_{n=1}^{\infty} F_n(\rho_a, r_0) \exp\left[-\kappa a_n^2 (\rho_a, r_0)\, t\right] , \tag{69}$$

where the coefficient F_n and eigen values a_n are both functions of ρ_a, the apparent density and r_0, the radius of the hollow spherical particle.

If we expand Eq. (69) where $\kappa a_n^2 t \ll 1$, and rearrange, we get

$$\overline{\theta}(t) \simeq \sum_{1}^{\infty} F_n(\rho_a, r_0)\, [1 - \kappa\, a_n^2 (\rho_a, r_0)\, t]$$

or

$$\overline{\theta}(t) \simeq \sum_{1}^{\infty} F_n(\rho_a, r_0) - \kappa \sum_{1}^{\infty} F_n(\rho_a, r_0)\, a_n^2(\rho_a, r_0)\, t . \tag{70}$$

From the initial condition (64), the first term in Eq. (70) converges to unity. If in the second term, the coefficient of t is set equal to β, then we have, from Eqs. (62) and (70),

$$\frac{\overline{T} - T_A}{T_m - T_A} = [1 - \beta(\rho_a, r_0)\, t] . \tag{71}$$

Equation (71) can be seen to be identical in form to Eq. (25) for the condition where $T_2 = 0$ in B. The parameter $\beta(\rho_a, r_0)$ determined on the basis of the analytical solution has been found to depend on ρ_a, and r_0 similarly to $\lambda(\rho_a, r)$ in Eq. (21a) within $1 < \rho_a < 3.5$, which is our range of interest. Hence the simpler heuristic approach is found satisfactory for the conditions of the problem.

BIBLIOGRAPHY

1. M. Plummer, "The Formation of Metastable Aluminas at High Temperatures," J. Appl. Chem. (London) 8, 35 (1958).
2. H. Meyer, "Das Verhalten von Pulvern im Plasmastrahl," Ber. Deut. Keram. Ges. 39 [2], 115 (1962).
3. J. H. Hollomon and D. Turnbull, "The Nucleation of the Solid," in A. I. M. and M. E. Symposium on The Solidification of Metals and Alloys, 1950, (American Institute of Mining and Metallurgical Engineers, New York, 1951), pp. 1-19.
4. J. D. Mackenzie, "Oxide Melts," in Advan. Inorg. Chem. Radiochem., 4, 295 (1962).
5. N. N. Ault, "Characteristics of Refractory Oxide Coatings Produced by Flame Spraying," J. Am. Ceram. Soc. 40, 69 (1957).
6. J. W. Newsome, H. W. Heiser, A. S. Russel, and H. C. Stumpf, "Alumina Properties," Alcoa Research Laboratories Technical Paper No. 10 (second revision), Alcoa, Pittsburgh, Pennsylvania, U.S.A., 1960, 88 pp.
7. M. Hoch and H. L. Johnston, "Formation, Stability, and Crystal Structure of the Solid Aluminum Suboxides: Al_2O and AlO," J. Am. Chem. Soc. 76, 2560 (1945).
8. Von K. Torkar and H. Krischner, "Neuere Arbeiten über Aluminiumoxyde," Ber. Deut. Keram. Ges. 39 [2], 131 (1962).
9. A. M. Kalinina, "Polymorphism of Aluminum Oxide and the Cause of Its Thermal Transitions," Zh. Neorgan. Khim. 4, 1260 (1959); Chem. Abstr. 54 [11], 10481b (1960).
10. A. L. Kozlovskii and K. S. Shlyakova, "Relation Between the Various Forms of Aluminum Oxides," Tr. Vses. Nauchn.-Issled. Inst. Avtogen. Obrabotki Metal. 6, 136 (1960); Chem. Abstr. 55 [17], 16062f (1961).
11. J. Frenkel, Kinetic Theory of Liquids (Dover Publications, Inc., New York, 1955), (a) p. 387; (b) p. 394, Eq. 24.
12. W. J. Dunning, "Theory of Crystal Nucleation from Vapour, Liquid and Solid Systems," in Chemistry of the Solid State, W. E. Garner, Ed. (Butterworths Scientific Publications, London, 1955), (a) p. 169, Eq. 50; (b) p. 170.

13. W. B. Hillig, "A Theoretical and Experimental Investigation of Nucleation Leading to Uniform Crystallization of Glass," in Symposium on Nucleation and Crystallization in Glasses and Melts (American Ceramic Society, Columbus, Ohio, 1962), pp. 77-89.

14. A. Kantrowitz, "Nucleation in Very Rapid Vapor Expansions," J. Chem. Phys. 19, 1097 (1951).

15. A. R. Das and R. M. Fulrath, Liquid-Solid Transformation Kinetics in Al_2O_3, Lawrence Radiation Laboratory Report UCRL-11166, December 1963; to be published in Proceedings of the 5th International Symposium on the Reactivity of Solids, August 5, 1964 (Elsevier Publishing Co., Amsterdam, Netherlands).

16. Roller Particle Size Analyzer Model No. 5-451, American Instrument Co., Silver Spring, Maryland, U.S.A.

17. R. R. John and W. L. Bade, "Recent Advances in Electric Arc Plasma Generation Technology," J. Am. Roc. Soc. 1, 4 (1961).

18. Direct Current Arc Plasma Jet Model No. F-40, Thermal Dynamics Corporation, Lebanon, New Hampshire, U.S.A.

19. J. D. Sullivan, Heavy Liquids for Mineralogical Analyses, U.S. Department of Commerce Technical Paper No. 381 (1927), 26 pp.

20. A. D. Krishenbaum and J. A. Cahill, "The Density of Liquid Aluminum Oxide," J. Inorg. Nucl. Chem. 14, 283 (1960).

21. H. P. Rooksby, "Preparation of Crystalline δ-Alumina," J. Appl. Chem. (London) 8, 44 (1958).

22. J. H. De Boer and G. M. M. Houben, "The Binding of Water In and On Aluminum Oxide," in Proceedings of the International Symposium on Reactivity of Solids, Gothenburg, 1952, (Elanders, Boktryckeri Aktiebolag, Göteborg, 1954), Part 1, pp. 237-44.

23. K. K. Kelly, U. S. Bureau of Mines, Berkeley, California, private communication.

24. W. D. Kingery, Introduction to Ceramics (John Wiley & Sons, Inc., New York, 1960), (a) p. 294; (b) pp. 497-98.

25. D. Turnbull, The Liquid State and the Liquid-Solid Transition, General Electric Research Laboratory, Schenectady, New York, Report No. 61-RL-2671M, 1961, p. 36, Table III.

26. W. B. Hillig and D. Turnbull, "Theory of Crystal Growth in Undercooled Pure Liquids," J. Chem. Phys. 24, 914 (1956).

27. B. J. McBride, S. Heimel, J. G. Ehlers, and S. Gordon, Thermodynamic Properties to 6000°K for 210 Substances Involving the First 18 Elements, National Aeronautics and Space Administration, Washington, D. C., No. NASA SP-3001, 1963, 328 pp.

28. R. Gardon, "The Emissivity of Transparent Materials," J. Am. Ceram. Soc. 39 [8], 278 (1956).

29. W. H. McAdams, Heat Transmission, Third Edition (McGraw-Hill Publications, New York, 1954), pp. 265-66.

30. H. S. Carlslaw and J. C. Jaeger, Conduction of Heat in Solids (Oxford University Press, London, 1959).